Master Thesis


# No identification of predicted earthquake-induced prompt gravity signals in data recorded by gravimeters, seismometers, and tiltmeters and its interpretation based on the principle of gravimetry

地震による即時重力変化の検出可能性の検討：既存モデルから期待される理論信号の加速度データ解析における不検出および重力計測原理に基づく解釈

**Masaya Kimura**


**Department of Earth & Planetary Science**
**Graduate School of Science, The University of Tokyo**

**February, 28, 2018**

# Abstract

Seismic waves radiated from an earthquake rupture induces density perturbations of the medium, which in turn generates prompt gravity changes at all distances before the arrival of seismic waves. Detection of the prompt gravity signal before the seismic one would contribute to early warning of earthquakes and is a challenge in seismology. Recent research have developed theoretical models of the transient gravity perturbations for earthquake faulting and reported the detection of such gravity signals prior to the P wave arrival from the 2011 Tohoku-Oki earthquake. In Chapter 2, we generalize the model and present analytical expressions for theoretical waveforms of gravity changes and its spatial gradients from a single force or a seismic moment tensor in an infinite homogeneous elastic medium. These formulae can be used to synthesize template waveforms and to find transient gravity changes in time-series data. In Chapter 3, we searched gravimetric data for such prompt gravity changes induced by the 2011 Mw 9.0 event using a band-pass filtering method. However, significant changes predicted by the theoretical model were not identified even though the data had sufficient signal-to-noise ratios. We also analyzed stacked broadband seismograph and tiltmeter array data and again could not detect the expected changes. To interpret the absence of signals in the data, we investigated the self-gravity effect on the measurement of gravitational acceleration, which has been ignored in the existing theory. For this purpose, we calculated the displacement of the observation station before P wave arrival, and showed that each point in the medium moves at an acceleration identical to the applied gravity change. This means that the above gravity sensors do not have sensitivity in principle to the prompt gravity change because of the opposite inertial force. Despite the

negative observability in acceleration, there remains possibility of detection in terms of its spatial gradients. The analytical expression for the theoretical gravity gradients we derived in Chapter 2 would contribute to future research.

# 要　旨

地震の動的な断層運動から放射される地震波は媒質の密度変化を引き起こし、それに起因する重力変化は光速度で伝わる。これは地震波に比して圧倒的な速度であり、重力変化は実質的に地震発生時刻から遅延時間ゼロで遠く離れた観測点にまで即時に到着することになる。もしこの「即時重力変化」の信号を地震波到達より先に捉えることができれば地震発生の早期検知に役立てることができ、その検出は地震学における課題である。近年、理論研究により地震断層が生み出す即時重力変化の無限均質等方弾性体中のモデルが提案された。また2011年東北沖地震によるP波到達前の重力信号の検出が報告された。本研究ではまず第二章において、この理論モデルを、シングルフォースやモーメントテンソルの一般的な震源に拡張し、それらから生じる即時変化から永久変化までの全ての時間に対する重力変化と重力勾配変化の理論記象の解析表現を導いた。これらの表現式により任意の震源による重力変化や重力勾配変化の波形テンプレートを合成でき、地震波到着に先立つ「即時信号」を時系列データの中から探すのに利用できる。次に第三章において我々は、2011年東北沖地震による即時重力信号を重力計データを用いて調べた。しかしながら、フィルタリング処理によって信号ノイズ比は十分に改善したにもかかわらず、理論モデルから期待される信号は一切見い出されなかった。更に、広帯域地震計データと傾斜計データを用いて、フィルター処理に加えて多点スタッキング処理も施したが、理論モデルから期待される信号は存在しなかった。観測データの中に理論モデルが予測する信号が記録されていない解析結果を説明するために、既存の理論

では無視されていた「自己重力の効果」が重力加速度測定に与える効果を理論的に調べた。地震発生からP波到達までの間に、「即時重力変化」それ自身が媒質に体積力として作用して地動変位を引き起こす効果を解析的に評価した。本研究で得た解析解は、媒質の各点は地震による重力変化と全く同じ加速度を持って運動することを示す。すなわち、重力加速度の計測中、センサー内のテストマス（重り）には重力変化と逆向きで同じ大きさの慣性力が働く。これは、重力計、地震計、傾斜計といった加速度センサーは即時重力変化に対して原理的に応答しなくなることを示している。本研究は、「即時重力変化」の加速度センサーによる検出が困難であることを示すが、その空間勾配の測定による検出の可能性は残されている。第二章で導いた一般震源に対する重力勾配変化の理論記象の解析表現は将来の信号検出に有用である。

# Contents

# Chapter 1. General introduction

　地震の断層運動は媒質の密度変化を生み出し、それは地球の重力場を変化させる。地震前後の「静的な重力変化」についてはこれまで理論モデルが構築され (Okubo 1991; 1992)、そのモデルが与える理論値は観測によって定量的に確かめられてきた (e.g., Tanaka et al., 2001; Imanishi et al., 2004)。この静的変化に加え、断層のコサイスミックな運動は地震発生直後から始まる「過渡的な重力変化」も引き起こすと期待される。重力変化は光速度という地震波に比べて圧倒的な速度で伝わるため、実質的に地震発生時刻から遅延時間ゼロで離れた観測点にも到着することになる。もし地震発生をこのP波より先に到来する「即時重力変化」で捉えることができれば地震の早期検知に役立てることができる (Harms et al., 2015) 。

　地震時の過渡的な重力変化については、近年Harms et al. (2015) が全無限均質等方弾性体中に置かれた点食い違いによる即時重力変化のモデルを構築し、その解析解を導いた。これによって地震発生からP波到達までの「即時重力変化」の理論波形を合成することができるようになった。そして、Montagner et al. (2016) は2011年東北沖地震によるP波到達前の重力信号を検出したと報告した。しかし、彼らの検出報告はP波直前のノイズレベルと地震非発生時の背景ノイズとの比較という統計的な手法によるものであり、Harms et al. (2015)の理論から予想される波形を発見したというものではなかった。地震学はこれまで観測波形と理論波形との一致という形で固体地球物理学でおきる現象を同定し理解

してきた。「即時重力変化」についても理論波形をデータの中に同定する形での検出が待たれている。

　我々はまず第二章において、Harms et al. (2015)の「点食い違い」が引き起こす「理論重力波形」の導出過程をたどり、これを一般的な点震源、つまりシングルフォースまたはモーメントテンソル、に拡張する。ここで重力変化・重力勾配変化の各理論波形の (i)モーメント関数依存性、および (ii) 震源–受信点距離の依存性が解析的に示され、理論地震波形との依存性の違いが意識される。我々は、全ての震源に対して、イベントの発生時刻から地震波到達、そして最終的な静的状態に至るまでの全ての過渡的応答の理論波形の解析的表現を導出した。この公式を用いて、代表的な３つの震源 (a) ダブルカップル：例として2011年東北沖地震、(b) シングルフォース：1980年セントヘレンズ火山噴火、及び (c) 特別な対称性を持つ震源：等方爆発、に対して重力変化と重力勾配変化の理論波形を合成した。2011年東北沖地震の「重力変化波形」は、点震源から放射される地震波と比べて際だって異なる性質を持つことが示される：(1) 即時重力変化の振幅は震源から離れた地点で最大値を持つ、(2) その距離は震源時間関数の継続時間と関係がある。これに対して「重力偏差波形」は地震波と同様に震源に近いほど振幅が大きくなる。この違いはそれぞれの波形の距離依存性の違いに起因する。ここで、M9規模の地震による「即時重力変化」は設置済みの重力計で十分に観測可能な信号レベルであることが示される。この理論波形に依拠した形で第三章ではデータ解析を行う。その他、物理的に興味深い結果として等方爆発は即時重力変化を生まずP波が到達して初めて重力が変化し始める、ことが理論的に示される。

第三章の前半部（データ解析）では、第二章で合成した理論波形と観測波形とを直接比較し、2011年東北沖地震による即時重力信号の検出を目指す。超伝導重力計（2点）、F-net広帯域地震計（71点）、Hi-net傾斜計（706点）という三種類の異なる測器により多点で記録されたデータの加速度成分を調べる。まず最初に、超伝導重力計のデータを調べる。バンドパスフィルタ処理によって脈動ノイズを十分に低減し、理論から期待される波形を探したがデータの中に理論波形を同定することはできなかった。次に、広帯域地震計と傾斜計の多点データを調べる。フィルター処理後のそれぞれのシングルチャンネルの波形には、理論波形の振幅は見いだせなかった。多点観測データの特徴を利用してスタッキング解析を追加で行ない理論モデルから予測される振幅の信号を探したが、再び結果は否定的であった。以上、我々が行ったデータ解析全てにおいて理論波形に基づく信号は見つからなかった。すなわち、我々のデータ解析は、既存理論モデルが観測データと矛盾することを強く示唆している。

　第三章の後半部（新たな観測モデル構築）では、第三章前半部で示唆された理論モデルとデータの間の矛盾を解決するために、Harms et al. (2015) の単純なモデルでは無視されていた「地球の自己重力の効果」を取り入れ、それが重力計測を行う観測サイト周辺の弾性変形に与える影響を定量的に調べる。この解析は既存モデルの解から初めて、その摂動展開として行う。まず、既存モデルでは、背景重力のない全無限均質媒質において、食い違いで生じる密度変化（P波フロント内部のみに分布）から即時重力変化（全空間に分布する体積力）が生まれる（状態1）。次に、新たに考える状態（状態2）として、状態1で生じた体積力が弾性体媒質に作用して生じる弾性体の変位場を動弾性体の表現定

理を用いて評価する。無限均質等方弾性媒質の場合、結果は解析的に得ることができる。結果は、一見して直感に反するものであった：P 波到達前の観測サイトの地動加速度はそこに働く即時重力変化と完全に一致する。これは重力測定において、重力計センサーの計測質量（test mass）に働く即時重力変化と地動加速度に伴う慣性力は、互いに完全に打ち消しあい、その結果加速度センサーの出力がゼロになることを意味する。すなわち、地震発生に伴い「即時重力変化」自体は生じるものの、重力計を設置した観測サイトもそれにより弾性変形を起こし同一の加速度で運動する結果、測定装置は「即時重力変化」に対して感度を失うのである。我々の考えたこの「新たな観測モデル」は、第三章前半部で明らかにした既存の理論モデルとデータ解析の間の矛盾を解決するものであると考える。

　第三章のDiscussionでは、地震の場合で導いた「即時重力変化と地動加速度が一致する」という上の結果が、実は地震時に特有の現象ではなく任意の密度変化の出現に対しても成り立つ、弾性体の本質的性質であることを重力相互作用と弾性体の性質から示す。また、我々の「新たな観測モデル」における無限均質媒質の仮定について指摘し、その仮定の破れがデータ解析結果に現れている可能性を議論する。その上で、我々の「新たな観測モデル」から示唆される地震即時重力変化検出の新たな研究の展開を議論する。観測者の加速後運動に依存せず測定可能な量である重力勾配変化の存在を指摘し、その観測可能性について今後の展望を述べる。そこでは第二章で導いた重力勾配変化の理論波形の表式は、今後の検出においてのテンプレート波形としての有用性が強調される。

# References

Harms, J., J. P. Ampuero, M. Barsuglia, E. Chassande-Mottin, J. P. Montagner, S. N. Somala, and B. F. Whiting (2015), Transient gravity perturbations induced by earthquake rupture, *Geophys. J. Int.*, *201*(3), 1416–1425, doi:10.1093/gji/ggv090.

Imanishi, Y., T. Sato, T. Higashi, W. Sun, and S. Okubo (2004), A network of superconducting gravimeters detects submicrogal coseismic gravity changes., *Science*, *306*(5695), 476–8, doi:10.1126/science.1101875.

Montagner, J.-P., K. Juhel, M. Barsuglia, J. P. Ampuero, E. Chassande-Mottin, J. Harms, B. Whiting, P. Bernard, E. Clévédé, and P. Lognonné (2016), Prompt gravity signal induced by the 2011 Tohoku-Oki earthquake, *Nat. Commun.*, *7*, 13349, doi:10.1038/ncomms13349.

Okubo, S. (1991), Potential and gravity changes raised by point dislocations, *Geophys. J. Int.,* 105(3), 573-586.

Okubo, S. (1992), Gravity and potential changes due to shear and tensile faults in a half-space, *J. Geophys. Res.*, 97, 7137-7144.

Tanaka, Y., S. Okubo, M. Machida, I. Kimura, and T. Kosuge (2001), First detection of absolute gravity change caused by earthquake, *Geophys. Res. Lett.*, *28*(15), 2979–2981.

# Chapter 2

# Theoretical waveforms of gravity and gravity-gradient changes associated with seismic sources

**SUMMARY**

Seismic waves radiated from diverse source processes accompany density perturbations, which give rise to transient gravity perturbations. Here we present analytical expressions for theoretical gravity and gravity-gradient changes associated with seismic radiations from a single force or a seismic moment tensor in an infinite homogeneous elastic medium. These formulae functionally give template waveforms for the use of finding transient gravity changes in time-series data. As quantitative examples, we synthesize gravity changes and gravity-gradient changes for the 2011 Tohoku-Oki earthquake and the 1980 St. Helens volcano eruption.

## 1 Introduction

Seismic waves radiated from diverse source processes generally accompany density perturbations, which give rise to transient gravity perturbations. Theoretical models of such transient perturbations have been developed for earthquake faulting (Harms *et al.*, 2015; Harms, 2016, Figure 1). It is remarkable that the gravity perturbations arrive at any observation station on the Earth prior to the P-wave arrival (i.e., density-perturbation arrival) owing to the long-range and virtually instantaneous (speed-of-light) interaction

of gravitational forces (Figure 2). Accordingly, they are referred to as prompt gravity perturbations. Detecting their very small amplitude is a challenge for state-of-the-art instruments such as gravitational gradiometers (e.g., torsion-bar antennas, Ando *et al.*, 2010). These signals, if practically measurable, would be the fastest method of detecting earthquake occurrences and contribute to early warning of earthquakes and tsunamis (Harms *et al.*, 2015). Montangner *et al.* (2016) reported the search for this type of prompt signals in data recorded by a superconducting gravimeter and broadband seismometers from the 2011 Mw 9.0 Tohoku-Oki earthquake.

In this study, we extend the theoretical modeling of Harms *et al.* (2015) to (i) general seismic sources described by a single force or a moment tensor and (ii) the entire process from the origin time to the static state. Starting from the equivalence between a potential giving rise to a seismic compressional field and the resultant gravity potential perturbation (Harms *et al.*, 2015), we derive analytical expressions for the theoretical gravity and gravity-gradient changes associated with a single force or a moment tensor in an infinite homogeneous elastic medium.

There is increasing interest in detecting prompt gravity signals associated with seismic events (Harms *et al.*, 2015; Harms, 2016; Montangner *et al.*, 2016). Our equations functionally give template waveforms for various seismic sources, which will contribute to finding such changes in time-series data. We apply our formulae to examples of theoretical signals from representative seismic sources and discuss their characteristics. For the 2011 Tohoku-Oki event, the prompt signals of gravity perturbation are in the possible detection ranges of superconducting gravimeters, whereas prompt gravity-gradient perturbations will be measurable in future by state-of-the-art instruments such as torsion-bar antennas (Ando *et al.*, 2010; Shoda *et al*, 2014).
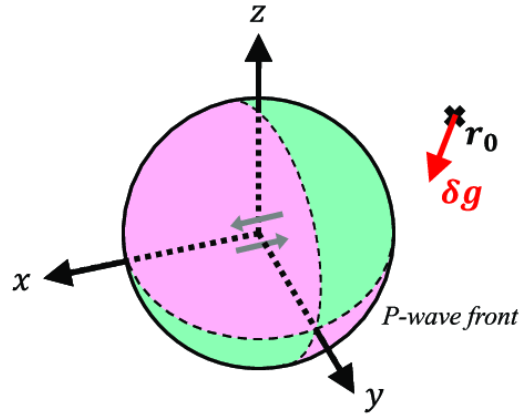
15

Figure 1: The fault slip at the origin and the source-based coordinates (xyz). The gravity change at a receiver outside the P wave front is induced by the distributed density perturbations inside the front.
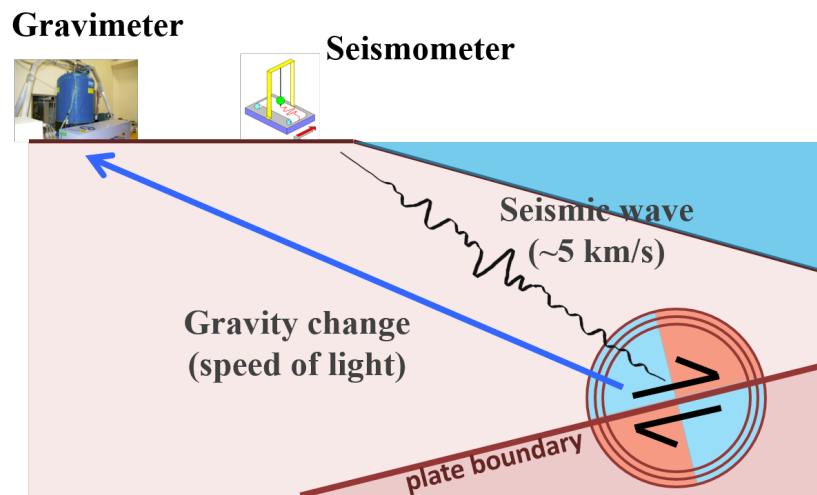


Figure 2: Schematic illustration of prompt gravity changes. Seismic waves propagate at the speed of P waves, and gravity changes propagate at the speed of light.

# 2 Derivation of theoretical gravity and gravity-gradient changes

We owe our model settings to Harms *et al.* (2015). They considered a shear-dislocation (double-couple) point-source in an infinite homogeneous isotropic elastic medium (Figure 1). They assumed that the deformation is related only to the point source and neglected coupling to the external static gravity field and self-gravity effects. Here we renew the source from the shear dislocation to a general point source described by a single force vector $F_p$ or a moment tensor $M_{pq}$ $(p, q = 1, 2, 3)$ and obtain equations for the resultant transient gravity and gravity-gradient perturbations.

## 2.1 Equivalence between seismic and gravity perturbation potentials

Our derivation starts from the equivalence between two potentials: one gives rise to a seismic compressional field; the other generates gravity potential perturbation (Harms *et al.,* 2015). We briefly summarize the equivalence.

A seismic displacement field $\boldsymbol{u}(\boldsymbol{x}, t)$ can be represented in term of its Lamé potentials (Aki & Richards, 2002):

$$\boldsymbol{u}(\boldsymbol{x}, t) = \nabla\phi(\boldsymbol{x}, t) + \nabla \times \boldsymbol{A}(\boldsymbol{x}, t)(= \boldsymbol{u}^\phi + \boldsymbol{u}^{\boldsymbol{A}}). \tag{1}$$

The scalar potential $\phi$ gives rise to compressional waves ($\nabla\phi(\boldsymbol{x}, t) = \boldsymbol{u}^\phi$), whereas the vector potential $\boldsymbol{A}$ produces shear waves ($\nabla \times \boldsymbol{A}(\boldsymbol{x}, t) = \boldsymbol{u}^{\boldsymbol{A}}$) obeying the condition $\nabla \cdot \boldsymbol{A} = 0$. In a homogeneous medium, the density perturbation field $\delta\rho(\boldsymbol{x}, t)$ is governed by the displacement:

$$\delta\rho(\boldsymbol{x}, t) = -\rho_0 \nabla \cdot \boldsymbol{u}(\boldsymbol{x}, t), \tag{2}$$

where $\rho_0$ is the unperturbed mass density. Inserting eq. (1) into eq. (2) yields

$$\delta\rho(\boldsymbol{x}, t) = -\rho_0 \nabla^2 \phi(\boldsymbol{x}, t). \tag{3}$$

On the other hand, the perturbation of the Newtonian gravity potential $\delta\psi(\boldsymbol{x}, t)$ is determined by the density perturbations according to Poisson's equation:

$$\nabla^2 \delta\psi(\boldsymbol{x}, t) = 4\pi G \delta\rho(\boldsymbol{x}, t), \tag{4}$$

where $G$ is the gravitational constant. From eq. (3) and eq. (4), $\nabla^2 \delta\psi = -4\pi G \rho_0 \nabla^2 \phi$. Thus, the equivalence

$$\delta\psi(\boldsymbol{x}, t) = -4\pi G \rho_0 \phi(\boldsymbol{x}, t) \tag{5}$$

is derived. Employing the well-known solution of seismic source potentials from a shear dislocation in an infinite medium (Aki & Richards, 2002), Harms *et al.* (2015) obtained an analytical expression for the prompt gravity perturbations $\delta\boldsymbol{g}(\boldsymbol{x}, t)$. They used the term "prompt" for the period from the event origin time $t = 0$ to the P-wave arrival time $t = r/\alpha$, where $\alpha$ is the P-wave velocity and $r$ is the distance between the source location $\boldsymbol{\xi}(= \boldsymbol{0})$ and receiver location $\boldsymbol{x}$.

## 2.2 Linkage between seismogram and gravity and gravity-gradient change via Lamé Potentials

Note that eq. (5) holds for any displacement field satisfying eq. (1). We thus apply eq. (1) and eq. (5) to (i) general seismic sources described by a single force $F_p$ or a moment tensor $M_{pq}$; and (ii) the entire process from the origin time to the static state. As a result, we obtain a simple and direct linkage between the displacement $\boldsymbol{u}(\boldsymbol{x}, t)$ and the gravity perturbation $\delta\boldsymbol{g}(\boldsymbol{x}, t)$.

From eq. (5), the gravity perturbation vector is represented by $\phi$:

$$\delta\boldsymbol{g}(\boldsymbol{x}, t) = -\nabla\delta\psi(\boldsymbol{x}, t) = 4\pi G \rho_0 \nabla\phi(\boldsymbol{x}, t). \tag{6}$$

Combining with eq. (1), we obtain the following relation

$$\delta\boldsymbol{g}(\boldsymbol{x}, t) = 4\pi G \rho_0 \boldsymbol{u}^\phi(\boldsymbol{x}, t). \tag{7}$$

This equation means that if we know the displacement described by Lamé potentials, we can directly obtain the corresponding gravity change by (i) extracting the scalar potential parts of the displacement field and by (ii) multiplying by a factor $4\pi G\rho_0$.

The corresponding gravity-gradient tenor (or strain acceleration tensor) is given as follows:

$$\ddot{h}_{nm}(\boldsymbol{x}, t) = \frac{\partial \delta g_n}{\partial x_m} = 4\pi G\rho_0 \frac{\partial u_n^\phi}{\partial x_m}. \tag{8}$$

This tensor is symmetric and has six different components. Equation (8) means that the gravity-gradient change is proportional to the spatial gradient of (the scalar potential parts of) the displacement, so we can obtain the gravity-gradient change by executing the following third step: (iii) differentiating with respect to the receiver coordinates.

In sections 2.3 to 2.5, we consider a moment-tensor source, which is a direct extension of a double couple of Harms *et al.* (2015). In section 2.6, equations for a single force are derived.

## 2.3 Expression of the gravity change associated with a moment tensor

From eq. (7), we obtain an analytical expression of the gravity change associated with a general moment tensor $M_{pq}(t)$. We employ the solution for the displacement vector $u_n(\boldsymbol{x}, t)$ in the source-based Cartesian coordinate system $(x_1, x_2, x_3)$ with origin at the

location of the point source (Aki & Richards, 2002):

$$
\begin{aligned}
u_n(\boldsymbol{x}, t) = \quad & M_{pq} * \frac{\partial G_{np}}{\partial \xi_q} \\
= \quad & \left( \frac{15\gamma_n\gamma_p\gamma_q - 3\gamma_n\delta_{pq} - 3\gamma_p\delta_{qn} - 3\gamma_q\delta_{np}}{4\pi\rho_0} \right) \frac{1}{r^4} \int_{r/\alpha}^{r/\beta} \tau M_{pq}(t - \tau) \, d\tau \\
& + \left( \frac{6\gamma_n\gamma_p\gamma_q - \gamma_n\delta_{pq} - \gamma_p\delta_{qn} - \gamma_q\delta_{np}}{4\pi\rho_0\alpha^2} \right) \frac{1}{r^2} M_{pq}(t - \frac{r}{\alpha}) \\
& - \left( \frac{6\gamma_n\gamma_p\gamma_q - \gamma_n\delta_{pq} - \gamma_p\delta_{qn} - 2\gamma_q\delta_{np}}{4\pi\rho_0\beta^2} \right) \frac{1}{r^2} M_{pq}(t - \frac{r}{\beta}) \\
& + \left( \frac{\gamma_n\gamma_p\gamma_q}{4\pi\rho_0\alpha^3} \right) \frac{1}{r} \dot{M}_{pq}(t - \frac{r}{\alpha}) - \left( \frac{\gamma_n\gamma_p\gamma_q - \gamma_q\delta_{np}}{4\pi\rho_0\beta^3} \right) \frac{1}{r} \dot{M}_{pq}(t - \frac{r}{\beta}) \quad (9) \\
= \quad & (u_n^\phi : \text{terms with } \alpha) + (u_n^{\boldsymbol{A}} : \text{terms with } \beta) \\
= \quad & M_{pq} * \frac{\partial G_{np}^\phi}{\partial \xi_q} + M_{pq} * \frac{\partial G_{np}^{\boldsymbol{A}}}{\partial \xi_q},
\end{aligned}
$$

where $*$ denotes the convolution integral in time, $\partial G_{np}/\partial \xi_q$ is the spatial derivative of the Green's tensor with respect to the source coordinates $\xi_q$, $\gamma_i (= (x_i - \xi_i)/r)$ is the directional cosine looking from the source, $\beta$ is the S-wave velocity, $\delta_{pq}$ is the Kronecker delta, and summation convention is applied. Terms with $\alpha$ come from the scalar potential; terms with $\beta$ are obtained from the vector potential. In seismology, different decaying terms with $1/r^4, 1/r^2$, and $1/r$ are referred to as near-field, intermediate, and far-field, respectively (Aki & Richards, 2002). Note that contributions from two potentials are combined in a single integral in the near-field term. They cancel out each other during the prompt period $0 \leq t \leq r/\alpha$, and thus the near-field term rises after the P-wave arrival.

Extracting the scalar potential contributions from eq. (9) and multiplying them by the coefficient $4\pi G\rho_0$, we obtain an expression of the theoretical gravity change $\delta g_n(\boldsymbol{x}, t)$:

$$
\begin{aligned}
\delta g_n(\boldsymbol{x}, t) = \quad & 4\pi G\rho_0 u_n^\phi = 4\pi G\rho_0 \left[ M_{pq} * \frac{\partial G_{np}^\phi}{\partial \xi_q} \right] \\
= \quad & -(15\gamma_n\gamma_p\gamma_q - 3\gamma_n\delta_{pq} - 3\gamma_p\delta_{qn} - 3\gamma_q\delta_{np}) \frac{G}{r^4} I_2[M_{pq}](t) \\
& + (6\gamma_n\gamma_p\gamma_q - \gamma_n\delta_{pq} - \gamma_p\delta_{qn} - \gamma_q\delta_{np}) \frac{G}{\alpha^2 r^2} M_{pq}(t - \frac{r}{\alpha}) \\
& + (\gamma_n\gamma_p\gamma_q) \frac{G}{\alpha^3 r} \dot{M}_{pq}(t - \frac{r}{\alpha}), \quad (10)
\end{aligned}
$$

where $I_2[M_{pq}](t)$ is related to $M_{pq}(t)$ as

$$I_2[M_{pq}](t) = \int_0^{r/\alpha} \tau M_{pq}(t - \tau)\, d\tau. \qquad (11)$$

For the prompt period, eq. (11) is identical to the second integral of the moment function $\int_0^t dt' \int_0^{t'} dt'' M_{pq}(t'')$ (Harms *et al.*, 2015). The first term of eq. (10) is responsible for the prompt response. The gravity change rises from $t = 0$ owing to the absence of the vector-potential contribution, as pointed out by Harms *et al.* (2015). The second and third terms are retarded by $(t - r/\alpha)$ and are proportional to $M_{pq}(t - r/\alpha)$ and $\dot{M}_{pq}(t - r/\alpha)$, respectively. In the gravity change, the transient dynamic response finishes at $t = r/\alpha + \tau_D$, where $\tau_D$ is the source duration time. The static gravity perturbation is represented by the first and second terms of eq. (10). For a given static moment $M_{pq}^\infty$, $I_2[M_{pq}](t)$ has a static value $(1/2)(r/\alpha)^2 M_{pq}^\infty$ for $t > r/\alpha + \tau_D$, and the first and second terms of eq. (10) have factors $GM_{pq}^\infty/(2\alpha^2 r^2)$ and $GM_{pq}^\infty/(\alpha^2 r^2)$, respectively.

## 2.4 Expression of the gravity-gradient change associated with a moment tensor

From eq. (8), we can gain an expression for the gravity-gradient change associated with a moment tensor $M_{pq}$. Using the equation

$$
\begin{aligned}
M_{pq} * \frac{\partial^2 G_{np}}{\partial \xi_m \partial \xi_q} = \quad & M_{pq} * \left[ \frac{\partial^2 G_{np}^\phi}{\partial \xi_m \partial \xi_q} + \frac{\partial^2 G_{np}^{\boldsymbol{A}}}{\partial \xi_m \partial \xi_q} \right] \\
= \quad & \frac{1}{4\pi\rho_0} \left[ R_5^\phi \frac{1}{r^5} I_2[M_{pq}](t) + R_3^\phi \frac{1}{\alpha^2 r^3} M_{pq}(t - \frac{r}{\alpha}) \right. \\
& \left. + R_2^\phi \frac{1}{\alpha^3 r^2} \dot{M}_{pq}(t - \frac{r}{\alpha}) + R_1^\phi \frac{1}{\alpha^4 r} \ddot{M}_{pq}(t - \frac{r}{\alpha}) \right] \\
& + \frac{1}{4\pi\rho_0} \left[ R_5^{\boldsymbol{A}} \frac{1}{r^5} I_2[M_{pq}](t) + R_3^{\boldsymbol{A}} \frac{1}{\beta^2 r^3} M_{pq}(t - \frac{r}{\beta}) \right. \\
& \left. + R_2^{\boldsymbol{A}} \frac{1}{\beta^3 r^2} \dot{M}_{pq}(t - \frac{r}{\beta}) + R_1^{\boldsymbol{A}} \frac{1}{\beta^4 r} \ddot{M}_{pq}(t - \frac{r}{\beta}) \right],
\end{aligned}
\qquad (12)
$$

where

$$
\begin{aligned}
R_5^\phi = \; & -105\gamma_n\gamma_p\gamma_q\gamma_m + 15(\delta_{mn}\gamma_p\gamma_q + \delta_{mp}\gamma_q\gamma_n + \delta_{mq}\gamma_n\gamma_p + \delta_{pq}\gamma_n\gamma_m + \delta_{qn}\gamma_p\gamma_m + \delta_{np}\gamma_q\gamma_m) \\
& -3(\delta_{pq}\delta_{nm} + \delta_{qn}\delta_{pm} + \delta_{np}\delta_{qm}), \\
R_3^\phi = \; & +45\gamma_n\gamma_p\gamma_q\gamma_m - 6(\delta_{mn}\gamma_p\gamma_q + \delta_{mp}\gamma_q\gamma_n + \delta_{mq}\gamma_n\gamma_p + \delta_{pq}\gamma_n\gamma_m + \delta_{qn}\gamma_p\gamma_m + \delta_{np}\gamma_q\gamma_m) \\
& +(\delta_{pq}\delta_{nm} + \delta_{qn}\delta_{pm} + \delta_{np}\delta_{qm}), \\
R_2^\phi = \; & 10\gamma_n\gamma_p\gamma_q\gamma_m - (\delta_{mn}\gamma_p\gamma_q + \delta_{mp}\gamma_q\gamma_n + \delta_{mq}\gamma_n\gamma_p + \delta_{pq}\gamma_n\gamma_m + \delta_{qn}\gamma_p\gamma_m + \delta_{np}\gamma_q\gamma_m), \\
R_1^\phi = \; & \gamma_n\gamma_p\gamma_q\gamma_m,
\end{aligned}
\tag{13}
$$

and

$$
\begin{aligned}
R_5^{\boldsymbol{A}} &= -R_5^\phi, \; R_3^{\boldsymbol{A}} = -R_3^\phi + 3\delta_{np}\gamma_q\gamma_m - \delta_{np}\delta_{qm}, \\
R_2^{\boldsymbol{A}} &= -R_2^\phi + 3\delta_{np}\gamma_q\gamma_m - \delta_{np}\delta_{qm}, \; R_1^{\boldsymbol{A}} = -R_1^\phi + \delta_{np}\gamma_q\gamma_m,
\end{aligned}
\tag{14}
$$

the expression of the gravity-gradient change is written as

$$
\begin{aligned}
\ddot{h}_{nm} &= \; 4\pi G\rho_0 \Big[ M_{pq} * \frac{\partial^2 G_{np}^\phi}{\partial x_m \partial \xi_q} \Big] \\
&= \; -4\pi G\rho_0 \Big[ M_{pq} * \frac{\partial^2 G_{np}^\phi}{\partial \xi_m \partial \xi_q} \Big] \\
&= \; -\Big[ R_5^\phi \frac{G}{r^5} I_2[M_{pq}](t, \frac{r}{\alpha}) + R_3^\phi \frac{G}{\alpha^2 r^3} M_{pq}(t - \frac{r}{\alpha}) \\
&\quad + R_2^\phi \frac{G}{\alpha^3 r^2} \dot{M}_{pq}(t - \frac{r}{\alpha}) + R_1^\phi \frac{G}{\alpha^4 r} \ddot{M}_{pq}(t - \frac{r}{\alpha}) \Big].
\end{aligned}
\tag{15}
$$

Note that $\partial G_{np}/\partial x_m = -\partial G_{np}/\partial \xi_m$. Similarly to the gravity change, the first term contains the prompt response and the other terms are retarded by $(t - r/\alpha)$. The first two terms have static values for $t > r/\alpha + \tau_D$ with factors $GM_{pq}^\infty/(2\alpha^2 r^3)$ and $GM_{pq}^\infty/(\alpha^2 r^3)$, respectively. Note that the distance decay rates of the prompt and static responses are one degree higher than those of the gravity change.

## 2.5 Density perturbation associated with a moment tensor

From eq. (2), the density perturbation field $\delta\rho(\boldsymbol{x}, t)$ is related to $u_n(\boldsymbol{x}, t)$:

$$
\begin{aligned}
\delta\rho(\boldsymbol{x}, t) &= -\rho_0 \nabla \cdot \boldsymbol{u}(\boldsymbol{x}, t) = -\rho_0 \nabla \cdot \boldsymbol{u}^\phi(\boldsymbol{x}, t) = -\rho_0 \left[ M_{pq} * \frac{\partial^2 G_{kp}^\phi}{\partial x_k \partial \xi_q} \right] \\
&= -\delta(\boldsymbol{x}) \frac{M_{kk}(t)}{3\alpha^2} + \frac{1}{4\pi} \left[ (3\gamma_p\gamma_q - \delta_{pq}) \frac{1}{\alpha^2 r^3} M_{pq}(t - \frac{r}{\alpha}) \right. \\
&\quad \left. + (3\gamma_p\gamma_q - \delta_{pq}) \frac{1}{\alpha^3 r^2} \dot{M}_{pq}(t - \frac{r}{\alpha}) + (\gamma_p\gamma_q) \frac{1}{\alpha^4 r} \ddot{M}_{pq}(t - \frac{r}{\alpha}) \right], \quad (16)
\end{aligned}
$$

where $\delta(\cdot)$ is Dirac's delta function. All terms are retarded by $(t - r/\alpha)$, and no prompt response exists because of the P-wave causality. Note that the first term represents the mass change at the origin. For $t > r/\alpha + \tau_D$, the static density field is represented by the first and second terms.

## 2.6 Expressions for a single force

The expressions for a single-force source are quite simple. We employ the solution for the displacement vector $u_n(\boldsymbol{x}, t)$ excited by a single force $F_p$ (Aki & Richards, 2002):

$$
\begin{aligned}
u_n(\boldsymbol{x}, t) &= F_p * G_{np} \\
&= \left( \frac{3\gamma_n\gamma_p - \delta_{np}}{4\pi\rho_0} \right) \frac{1}{r^3} \int_{r/\alpha}^{r/\beta} \tau F_p(t - \tau) \, d\tau \\
&\quad + \left( \frac{\gamma_n\gamma_p}{4\pi\rho_0\alpha^2} \right) \frac{1}{r} F_p(t - \frac{r}{\alpha}) - \left( \frac{\gamma_n\gamma_p - \delta_{np}}{4\pi\rho_0\beta^2} \right) \frac{1}{r} F_p(t - \frac{r}{\beta}). \quad (17)
\end{aligned}
$$

Extracting the scalar potential contributions from eq. (17) and multiplying them by $4\pi G\rho_0$, we obtain the expression for the theoretical gravity change:

$$
\begin{aligned}
\delta g_n(\boldsymbol{x}, t) &= 4\pi G\rho_0 u_n^\phi = 4\pi G\rho_0 \left[ F_p * G_{np}^\phi \right] \\
&= -(3\gamma_n\gamma_p - \delta_{np}) \frac{G}{r^3} I_2[F_p](t) + (\gamma_n\gamma_p) \frac{G}{\alpha^2 r} F_p(t - \frac{r}{\alpha}), \quad (18)
\end{aligned}
$$

where $I_2[F_p](t)$ is related to $F_p(t)$ as in eq. (11). The first term contains the prompt response and the second term is retarded by $(t - r/\alpha)$. Both terms remain static for

$t > r/\alpha + \tau_D$. For a given static force $F_p^\infty$, the two terms have static factors $GF_p^\infty/(2\alpha^2 r)$ and $GF_p^\infty/(\alpha^2 r)$, respectively.

Differentiating the gravity change with respect to the receiver coordinates, we obtain the expression of the gravity-gradient change:

$$
\begin{aligned}
\ddot{h}_{nm}(\boldsymbol{x}, t) = \quad & 4\pi G \rho_0 \frac{\partial u_n^\phi}{\partial x_m} = 4\pi G \rho_0 \left[ F_p * \frac{\partial G_{np}^\phi}{\partial x_m} \right] \\
= \quad & (15\gamma_n \gamma_p \gamma_m - 3\gamma_n \delta_{pm} - 3\gamma_p \delta_{mn} - 3\gamma_m \delta_{np}) \frac{G}{r^4} I_2[F_p](t) \\
& -(6\gamma_n \gamma_p \gamma_m - \gamma_n \delta_{pm} - \gamma_p \delta_{mn} - \gamma_m \delta_{np}) \frac{G}{\alpha^2 r^2} F_p(t - \frac{r}{\alpha}) \\
& -(\gamma_n \gamma_p \gamma_m) \frac{G}{\alpha^3 r} \dot{F}_p(t - \frac{r}{\alpha}).
\end{aligned}
\tag{19}
$$

Note that owing to the relation $\partial G_{np}/\partial \xi_m = -\partial G_{np}/\partial x_m$, this expression can be obtained by replacing $q$ with $m$ in eq. (10) and by reversing the sign. The first term contains the prompt response and the last two are retarded by $(t - r/\alpha)$. The static response for $t > r/\alpha + \tau_D$ is given by the first two terms, which have static factors $GF_p^\infty/(2\alpha^2 r^2)$ and $GF_p^\infty/(\alpha^2 r^2)$, respectively.

The density perturbation field $\delta\rho(\boldsymbol{x}, t)$ resulting from eq. (17) is given as follows:

$$
\begin{aligned}
\delta\rho(\boldsymbol{x}, t) = \quad & -\rho_0 \nabla \cdot \boldsymbol{u}^\phi(\boldsymbol{x}, t) = -\rho_0 \left[ F_p * \frac{\partial G_{kp}^\phi}{\partial x_k} \right] \\
= \quad & \frac{\gamma_p}{4\pi\alpha^2} \left[ \frac{1}{r^2} F_p(t - \frac{r}{\alpha}) + \frac{1}{\alpha r} \dot{F}_p(t - \frac{r}{\alpha}) \right].
\end{aligned}
\tag{20}
$$

Both terms are retarded by $(t - r/\alpha)$, and no prompt term exists because of the P-wave causality. The first term gives the static factor $F_p^\infty/(4\pi\alpha^2 r^2)$ for $t > r/\alpha + \tau_D$.

# 3 Examples

Assuming three types of seismic processes, we examine the characteristics of transient gravity perturbations and their gradients. We employ spherical coordinates $(r, \theta, \varphi)$ related to Cartesian coordinates via $x_1 = r \sin\theta \cos\varphi$, $x_2 = r \sin\theta \sin\varphi$, $x_3 = r \cos\theta$, with $0 \le \theta \le \pi$ and $0 \le \varphi \le 2\pi$.

## 3.1 Earthquake gravity and gravity-gradient change

Most seismograms result from earthquakes. Following Harms *et al.* (2015), we consider shear faulting with a slip vector $\Delta \boldsymbol{u} = (\Delta u, 0, 0)$ on a fault $\Gamma$ on the $x_1 - x_2$ plane with its normal vector $\boldsymbol{n} = (0, 0, 1)$ (Figure 1). This seismic source is represented by a moment tensor with non-zero components $M_{13} = M_{31} = M_0(t)$, i.e., a double couple (Aki & Richards, 2002). $M_0(t)$ is a moment function that increases from zero to static seismic moment $M_0^\infty$ with a duration time $\tau_D$.

From eq. (10), the expression of the gravity change is

$$
\begin{aligned}
\delta g_n(\boldsymbol{x}, t) = \quad & (-30\gamma_1\gamma_3\gamma_n + 6\gamma_1\delta_{3n} + 6\gamma_3\delta_{1n})\frac{G}{r^4}I_2[M_0](t) \\
& +(12\gamma_1\gamma_3\gamma_n - 2\gamma_1\delta_{3n} - 2\gamma_3\delta_{1n})\frac{G}{\alpha^2 r^2}M_0(t - \frac{r}{\alpha}) \\
& +(2\gamma_1\gamma_3\gamma_n)\frac{G}{\alpha^3 r}\dot{M}_0(t - \frac{r}{\alpha}).
\end{aligned} \tag{21}
$$

The first term includes a prompt response and agrees with the prompt term of Harms *et al.* (2015). After $t > r/\alpha + \tau_D$, the third term is equal to zero and the others have static factors $GM_0^\infty/(2\alpha^2 r^2)$ and $GM_0^\infty/(\alpha^2 r^2)$, respectively. The static values can be compared with the static solution in a homogeneous half-space (Okubo, 1991). The equation written in a vector form helps us gain physical insights:

$$
\delta \boldsymbol{g}(\boldsymbol{x}, t) = -\boldsymbol{A}^N \frac{G}{r^4}I_2[M_0](t, \frac{r}{\alpha}) + \boldsymbol{A}^{IP}\frac{G}{\alpha^2 r^2}M_0(t - \frac{r}{\alpha}) + \boldsymbol{A}^{FP}\frac{G}{\alpha^3 r}\dot{M}_0(t - \frac{r}{\alpha}), \tag{22}
$$

where

$$
\begin{aligned}
\boldsymbol{A}^N = \quad & 9\sin 2\theta \cos\varphi \boldsymbol{e_r} - 6(\cos 2\theta \cos\varphi \boldsymbol{e_\theta} - \cos\theta \sin\varphi \boldsymbol{e_\varphi}) = 9\boldsymbol{A}^{FP} - 6\boldsymbol{A}^{FS} \\
\boldsymbol{A}^{IP} = \quad & 4\sin 2\theta \cos\varphi \boldsymbol{e_r} - 2(\cos 2\theta \cos\varphi \boldsymbol{e_\theta} - \cos\theta \sin\varphi \boldsymbol{e_\varphi}) = 4\boldsymbol{A}^{FP} - 2\boldsymbol{A}^{FS} \\
\boldsymbol{A}^{FP} = \quad & \sin 2\theta \cos\varphi \boldsymbol{e_r} \\
\boldsymbol{A}^{FS} = \quad & \cos 2\theta \cos\varphi \boldsymbol{e_\theta} - \cos\theta \sin\varphi \boldsymbol{e_\varphi}.
\end{aligned} \tag{23}
$$

In seismology, $\boldsymbol{A}^N$, $\boldsymbol{A}^{IP}$, $\boldsymbol{A}^{FP}$, and $\boldsymbol{A}^{FS}$ denote the radiation patterns (particle

displacement vectors) of the near-field, intermediate P-, and far-field P- and far-field S-waves, respectively (Aki & Richards, 2002). $\boldsymbol{A}^{N}$ and $\boldsymbol{A}^{IP}$ are composed of $\boldsymbol{A}^{FP}$ (= radial component) and $\boldsymbol{A}^{FS}$ (= transverse component).

The radiation pattern of gravity perturbations can be understood in terms of the density distribution

$$\delta\rho(\boldsymbol{x}, t) = \frac{R_p(\theta, \varphi)}{4\pi\alpha^2} \left[ \frac{3}{r^3} M_0(t - \frac{r}{\alpha}) + \frac{3}{\alpha r^2} \dot{M}_0(t - \frac{r}{\alpha}) + \frac{1}{\alpha^2 r} \ddot{M}_0(t - \frac{r}{\alpha}) \right], \quad (24)$$

where $R_p(\theta, \varphi)(= \sin 2\theta \cos \varphi = 2\gamma_1\gamma_3)$ represents the P-wave radiation pattern. Therefore, the density perturbation spreads with the well-known quadrant pattern. Owing to this quadratic density distribution, attractive and compulsive forces from the source act in the plane $\{\theta = \pi/4, -\pi/4\}$ as shown in Figure 3a, whereas the symmetry in turn causes rotational forces in the plane $\{\theta = 0, \pi/2\}$, as illustrated in Figure 3b. For intermediate directions, combined forces act. The gravity perturbations vary with time depending on $I_2[M_0](t)$, $M_0(t - r/\alpha)$ and $\dot{M}_0(t - r/\alpha)$.
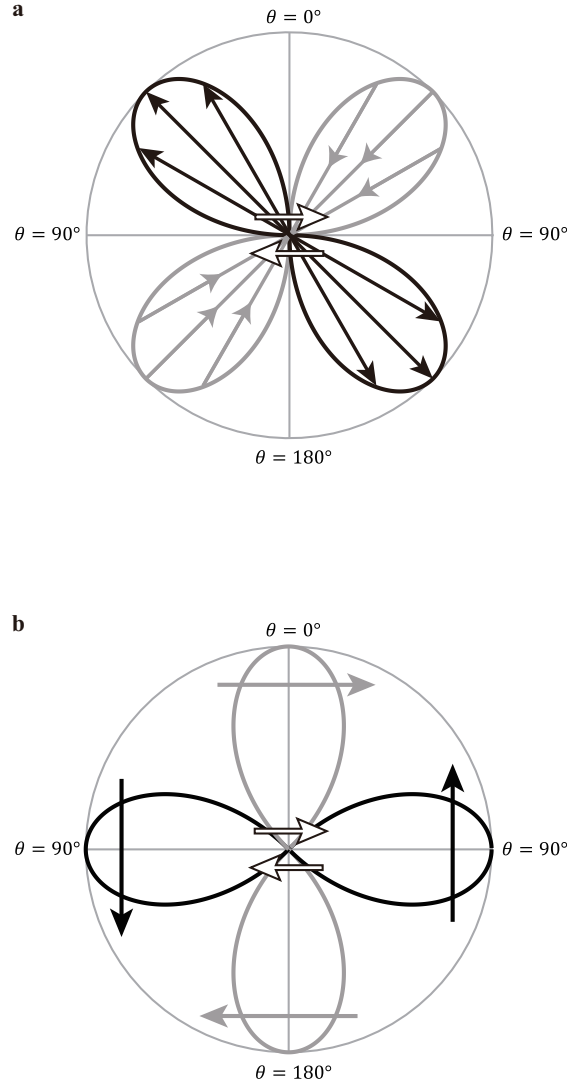
Figure 3: (a) Diagrams for the radiation pattern of the radial component of gravity perturbation due to a double couple, i.e., $-\sin 2\theta \cos \varphi \boldsymbol{e_r}$. The diagram is for a plane of constant $\varphi$, and the pair of arrows at the center denotes the shear dislocation. Note the alternating quadrants of inward and outward directions. (b) Diagram for the radiation pattern of the transverse component of gravity perturbation due to a double couple, i.e., $\cos 2\theta \cos \varphi \boldsymbol{e_\theta} - \cos \theta \sin \varphi \boldsymbol{e_\phi}$. This is the four-lobed pattern in the plane $\{\varphi = 0, \varphi = \pi\}$. The lobes are a locus of points at a distance from an origin that is proportional to $\cos 2\theta$. Arrows imposed on each lobe show the direction of gravity perturbation.

As a quantitative example, we synthesize gravity and gravity-gradient waveforms for the 2011 Tohoku-Oki earthquake (Mw 9.0). The seismic source is represented by a moment tensor located at the hypocenter. We employ a mechanism (strike= $201°$, dip= $10°$, rake= $90°$) and moment-rate function following Wei *et al.* (2012) and hypocenter coordinates (38.19°N, 142.68°E, depth 21 km) following Chu *et al.* (2011). The moment-rate function has a duration $\tau_D = 300$ s, but the moment release almost finishes at 150 s (Figure 4). We employ a constant P-wave velocity ($\alpha = 7$ km/s) in the homogeneous model, and the model arrival time is given by $t_p = r/\alpha$ for a source-receiver distance $r$, which approximates the observed arrival time.

Figures 5 and 6 show the gravity waveforms in three components and gravity-gradient waveforms in six components for the Kamioka Observatory ($r = 515$ km, $t_p = 74$ s), respectively. During the prompt period, all waveforms increase/decrease monotonically. The transient waveforms continue after P-wave arrival, and finally reach static values at about $t = 350$ s ($\simeq t_p + \tau_D$). The maximum amplitude in the prompt part of the gravity changes is $-3.5 \times 10^{-8}$ m/s$^2$ in the $\delta g_3$ component, whereas the static change is approximately $-17 \times 10^{-8}$ m/s$^2$ ($10^{-8}$ m/s$^2$ = 1 micro Galileo, about $10^{-9}$ times the surface gravity acceleration). In the gravity waveforms, the prompt changes are a fraction of the static changes. For the gravity-gradient waveforms, the maximum in the prompt parts is approximately $-2 \times 10^{-13}$ s$^{-2}$ in the $\ddot{h}_{13}$ component, whereas the static change is approximately $-5 \times 10^{-13}$ s$^{-2}$.

From the viewpoint of instrumental measurements, the theoretical waveforms in the post-prompt period may make no sense; the receiver sites start to shake, which disturbs the calm situation required for high-precision measurements.
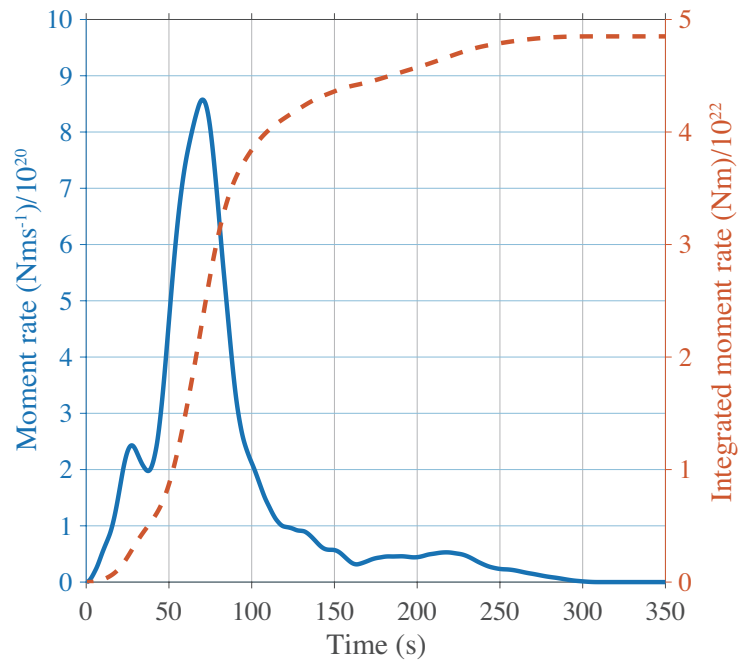
Figure 4: Seismic moment (dashed line) and moment rate (solid line) time-functions of the Tohoku-Oki earthquake (Wei *et al.*, 2012).
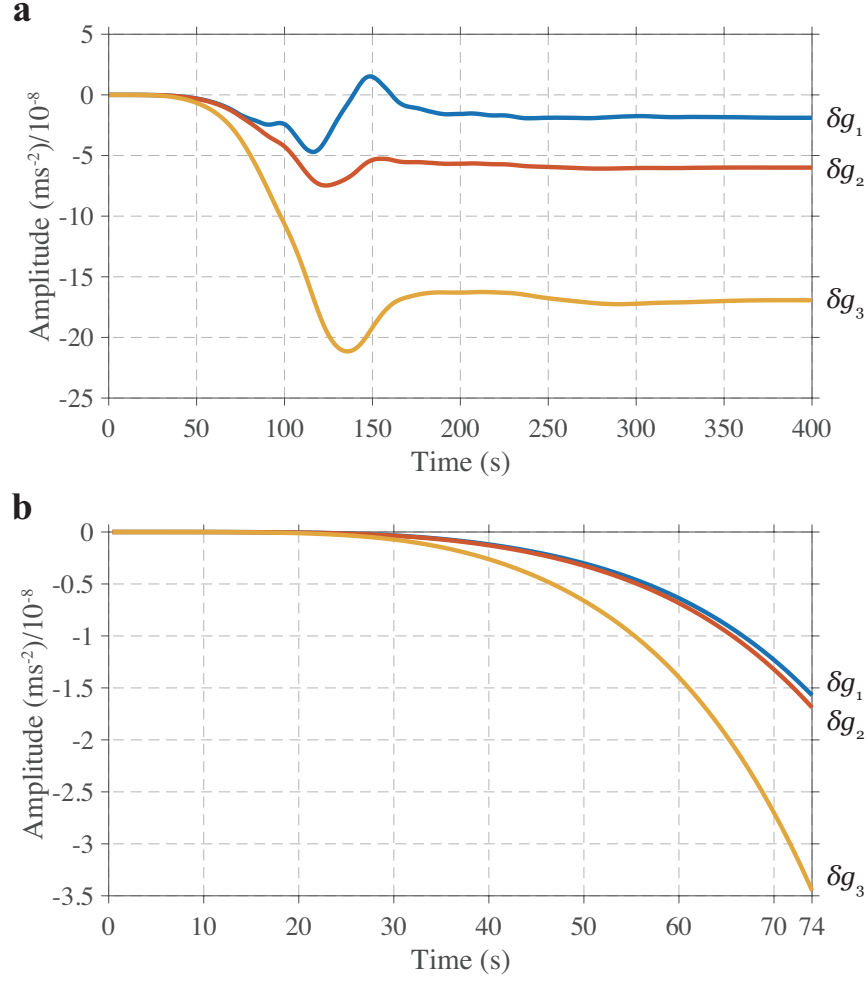
Figure 5: Theoretical three-component gravity waveforms of the 2011 Tohoku-Oki earthquake synthesized for Kamioka Observatory ($r = 515$ km) where the prompt period is from $t = 0$ s (the origin time) to $t_p = 74$ s (P-wave arrival time). $(x_1, x_2, x_3)$ coordinates are taken in the directions $(EW, NS, UD)$ with $ENU$ positive. (a) Whole gravity changes for $0 < t < 400$ s. (b) Enlarged view for $0 < t < 74$ s($= t_p$).
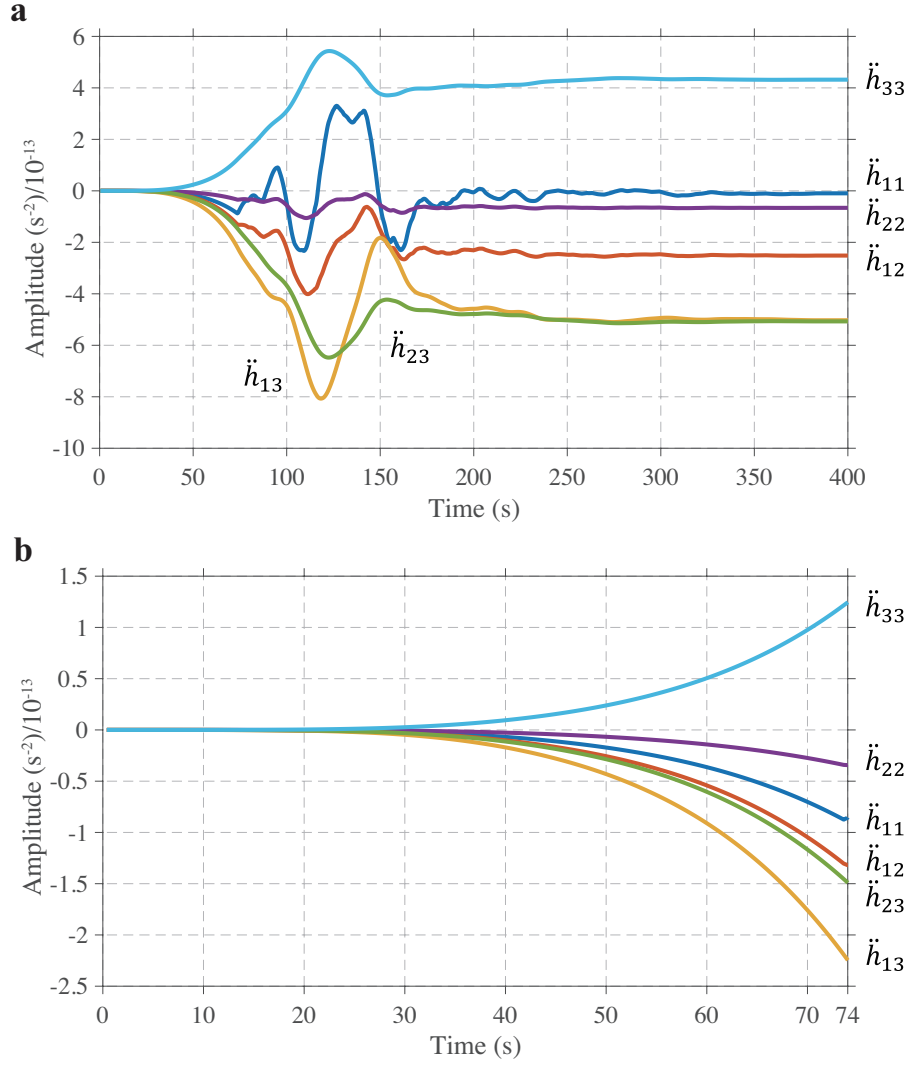
Figure 6: Theoretical six-component gravity-gradient waveforms of the 2011 Tohoku-Oki earthquake synthesized for Kamioka Observatory. (a) Whole gravity-gradient changes for $0 < t < 400$ s. (b) Enlarged view for $0 < t < 74$ s$(= t_p)$.

Note that we have assumed a point-source approximation. For this 2011 event, the whole seismograms recorded by the broadband nationwide network F-net have been well explained by a point source between 0.02 and 0.06 Hz because the major moment release has been estimated to occur in a narrow region with radius 70 km in a short duration of 40 s (Kumagai *et al.*, 2012). This finding suggests that the signs and orders of the prompt signals with monotonically increasing characteristics would hold even if we consider a finite fault model.

We next examine the relationship between the receiver location and the prompt signal amplitude expected at the location, which is crucial for prompt detection of earthquake occurrence. As shown in eq. (22), the prompt term consists of $I_2[M_0](t)$, which monotonically increases in time during the prompt period $0 < t < r/\alpha$. Thus, the prompt signals attained in the gravity and gravity-gradient changes are proportional to $GI_2[M_0](r/\alpha)/r^4$ and $GI_2[M_0](r/\alpha)/r^5$, respectively (omitting radiation patterns).

Figure 7 shows $GI_2[M_0]/r^4$ and $GI_2[M_0]/r^5$ as a function of $r$. $GI_2[M_0]/r^4$ has a peak around $r = 750$ km: the gravity perturbation at P-wave arrival increases for distances smaller than 750 km. This is because the moment function rises quickly during the beginning of the event, as pointed out by Montagner *et al.* (2016). The peak time $t \simeq 100$ s corresponds to the time when inclination of the moment function becomes lower (Figure 4). For the gravity-gradient changes, $GI_2[M_0]/r^5$ monotonically decays with $r$ owing to the one-degree higher decay rate. In this case, $GI_2[M_0]/r^5$ diverges when $r$ approaches to zero, which is caused by the point source approximation and would never occur in a finite fault model. The behavior of the two functions suggests that if we approximate the initial rise of the employed moment function by $t^n$, $n$ is estimated as $2 < n < 3$. If the initial rise in the moment function is $n > 3$, the gradient of the gravity perturbation at P-wave arrival would have a spatial peak as for the gravity perturbation.

Combining the radiation coefficients with the above distance-dependent functions, we obtain the distributions of the prompt signal amplitudes at P-wave arrival (Figure 8). For the gravity changes, there are quadratic patterns in the $\delta g_1$ and $\delta g_2$ components and an anti-symmetric pattern in the $\delta g_3$ component (Figure 8a). The maximum signals
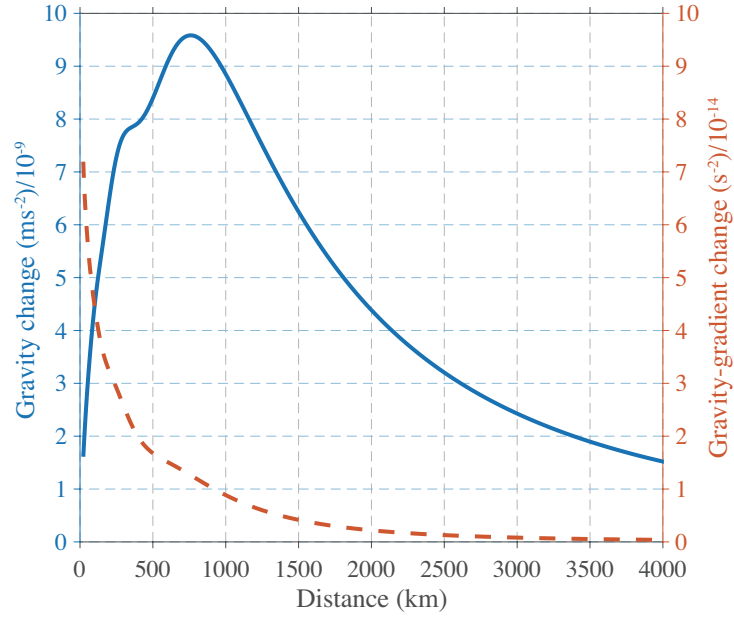
Figure 7: Plots of $GI_2[M_0]/r^4$ (solid line) and $GI_2[M_0]/r^5$ (dashed line) associated with the 2011 Tohoku-Oki earthquake. They show reference signal levels (without radiation coefficients) at receiver distances ($r$) greater than 21 km.

($\simeq \pm 5 \times 10^{-8}$ m/s$^2$) take place in the $\delta g_3$ component at a distance $r \simeq 750$ km. The amplitude of $5 \times 10^{-8}$ m/s$^2$ is large enough to measure with superconducting gravimeters. In fact, static gravity changes of less than $10^{-8}$ m/s$^2$ due to earthquakes have been identified with high-resolution gravity recordings (e.g., Tanaka et al., 2001; Imanishi *et al.*, 2004). Dynamic detection seems to be a realistic challenge, though difficulties would arise in identifying waveforms: there is rich background microseism noise, which always contaminates signals as short-period time-oscillating noise.

In the gravity-gradient changes, there are more complicated patterns in a narrower range (Figure 8b). The maximums on the surface ($r > 21$ km) are on the order of $10^{-13}$ s$^{-2}$ in each component. This value, $10^{-13}$ s$^{-2}$, is about five orders below the attained sensitivity of a prototype torsion-bar antenna between $0.01$ and $0.1$Hz (Shoda *et al.*, 2015). A next generation torsion-bar antenna will be developed to attain high sensitivity below $10^{-13}$s$^{-2}$ (Ando, personal communication).
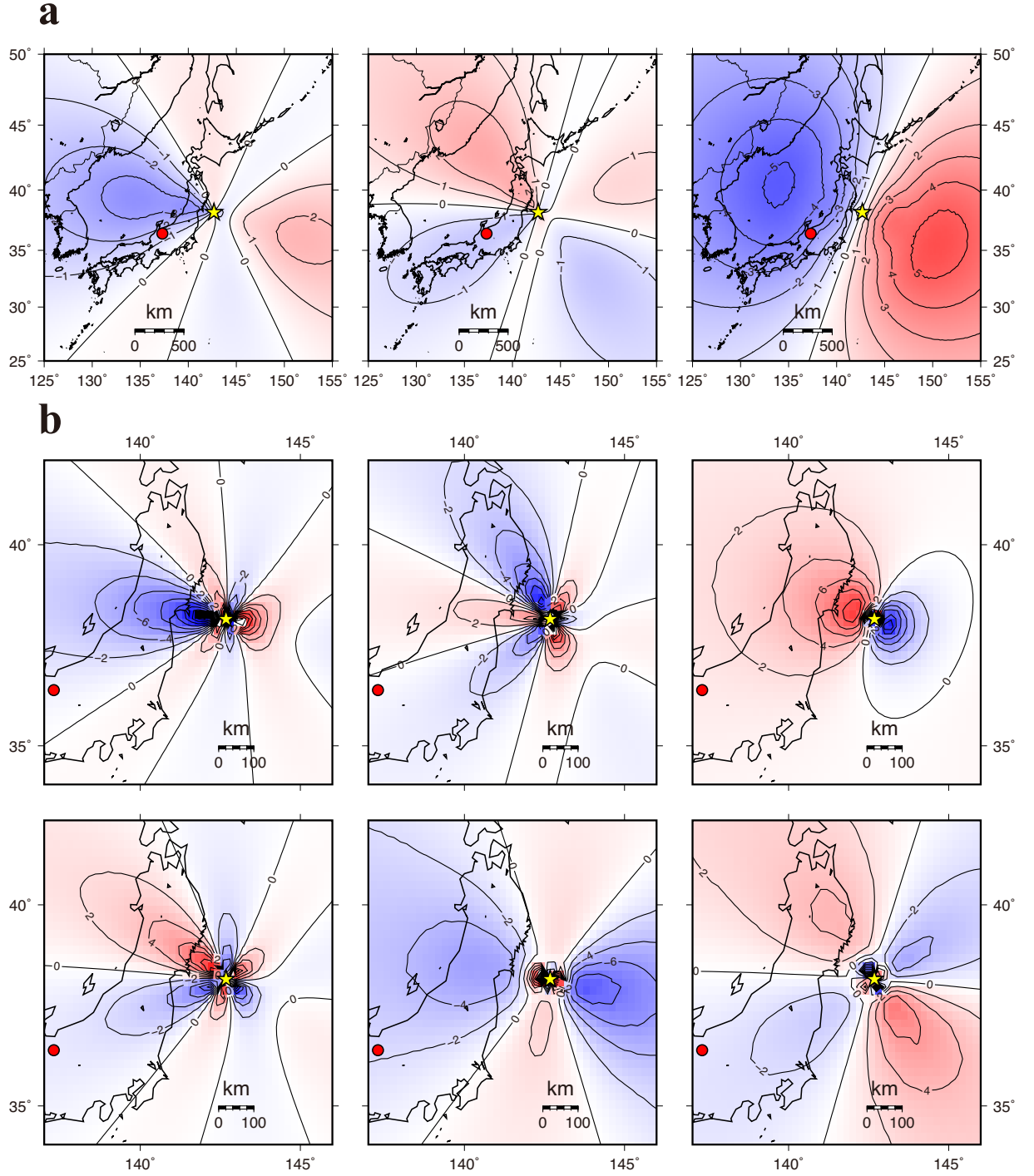
Figure 8: (a) Distributions of prompt gravity changes immediately before the P-wave arrival at each location (left: $x_1$ component, center: $x_2$, right: $x_3$). The star and circle symbols indicate the hypocenter of the 2011 Tohoku-Oki earthquake and Kamioka Observatory, respectively. Red and blue colors indicate positive and negative changes, respectively. The contour lines are drawn at every $10^{-8}$ m/s$^2$. (b) Distributions of prompt gravity-gradient changes immediately before the P-wave arrival at each location (upper left: $\ddot{h}_{11}$ component, upper center: $\ddot{h}_{22}$, upper right: $\ddot{h}_{33}$, lower left: $\ddot{h}_{12}$, lower center: $\ddot{h}_{13}$, lower right: $\ddot{h}_{23}$). The contour lines are drawn at every $2 \times 10^{-13}$ s$^{-2}$.

## 3.2   Isotropic expansion

An interesting exception in seismic sources is isotropic expansion for which prompt gravity perturbations disappear. The source process is represented by a moment tensor with non-zero components $M_{11} = M_{22} = M_{33} = M_0(t)$. When a growing spherical cavity with a static volume change $\Delta V$ (or a static overpressure $\Delta P$) is considered, the static moment is given as follows: $M_0^{\infty} = (\lambda + 2\mu)\Delta V = (2 + \lambda/\mu)\pi R^3 \Delta P$, where $\lambda$ and $\mu$ is the Lamè constant of the surrounding medium and $R$ is the radius of the cavity (e.g., Kumagai *et al.*, 2014, Ichihara *et al.*, 2016).

With the summation $(p, q) = (1, 1), (2, 2), (3, 3)$ in eq. (10), we obtain the gravity perturbations:

$$\delta \boldsymbol{g}(\boldsymbol{x}, t) = \frac{G}{\alpha^2 r^2} M_0(t - r/\alpha)\boldsymbol{e_r} + \frac{G}{\alpha^3 r} \dot{M}_0(t - r/\alpha)\boldsymbol{e_r}. \tag{25}$$

Because of the spherical symmetry, gravity perturbations depend only on $r$, have only a radial component, and the radiation coefficient of the $I_2$ term is zero. Thus, the gravity perturbations propagate only with the P-wave velocity, not with the speed of light.

We can gain physical insights from the density perturbation distribution. From eq. (16),

$$\delta \rho(\boldsymbol{x}, t) = -\delta(\boldsymbol{x})\frac{M_0(t)}{\alpha^2} + \frac{1}{4\pi\alpha^4 r}\ddot{M}_0(t - \frac{r}{\alpha}). \tag{26}$$

The first term shows time-varying mass deficient $\delta m_-(t)(= -M_0(t)/\alpha^2)$ at the origin. The second term shows the mass compensation $\delta m_+(t)(= M_0(t)/\alpha^2)$ radiated from the origin. The positive mass $\delta m_+(t)$ can be calculated by integrating the second term of eq. (26) in the region $+0 < r < \alpha t$. Before P-waves arrive at a receiver, the spherically distributed mass can be regarded as a concentrated mass at the origin. As a result, the effective mass change is zero and no gravity change appears. For the post prompt period $r/\alpha < t < r/\alpha + \tau_D$, the P-waves are passing the receiver and the effective mass becomes negative because the spherically distributed positive mass outside the receiver induces no gravity changes. For the static period $t > r/\alpha + \tau_D$, the gravity perturbations without the effect of the compensating positive mass become $\delta \boldsymbol{g}(\boldsymbol{x}, \infty) = -G\frac{(-M_0^{\infty}/\alpha^2)}{r^2}\boldsymbol{e_r}$,

indicating Newton's law of gravitation ($1/r^2$ decay) associated with the static mass deficient $\delta m_-^\infty = -M_0^\infty/\alpha^2$. Note that the static gravity perturbations are a compulsive force, not an attractive force, because of the negative mass change at the origin.

## 3.3 Volcanic eruption

A volcanic eruption is an example of a single-force seismic source (e.g., Kanamori & Given, 1983). We consider a simple source model in which only a vertical force $F_3$ acts at the origin. The source-time function $F_3(t) = -f(t) = -(F_0/2)(1 - \cos(2\pi/\tau_D)t)$ is assumed, with a constant $F_0$ and a duration $\tau_D$. $f(t)$ has a peak $F_0$ at $t = \tau_D/2$ and returns to 0 at $t = \tau_D$. From eq. (18) with $p = 3$, the expression of the gravity change is

$$\delta \boldsymbol{g}(\boldsymbol{x}, t) = (-2\cos\theta \boldsymbol{e_r} - \sin\theta \boldsymbol{e_\theta})\frac{G}{r^3}I_2[F_3](t) + (\cos\theta \boldsymbol{e_r})\frac{G}{\alpha^2 r}F_3(t - \frac{r}{\alpha}). \qquad (27)$$

The first term contains a prompt response and the second is retarded by $(t - r/\alpha)$. Both terms have static factors $GF_3^\infty/(2\alpha^2 r^2)$ and $GF_3^\infty/(\alpha^2 r^2)$, respectively. The expression of the density change is

$$\delta\rho(\boldsymbol{x}, t) = \frac{\cos\theta}{4\pi\alpha^2}\left[\frac{1}{r^2}F_3(t - \frac{r}{\alpha}) + \frac{1}{\alpha r}\dot{F}_3(t - \frac{r}{\alpha})\right]. \qquad (28)$$

Parallel expression of the gravity-gradient change can be obtained from eq. (19), and each tensor component has a prompt term with a factor $GI_2[F_3]/r^4$. The tensor form is cumbersome and omitted for brevity.

As a quantitative example, we consider the prompt signals from the 1980 St. Helens eruptions. Of these events, that of 13 June was well modeled by a single pulse with momentum and duration. The 18 May event was the largest, with momentum $1.4 \times 10^{14}$ N $\cdot$ s and duration $25$ s (Kanamori & Given, 1983). The source-time function was not well constrained by the observed seismograms, so herein we arbitrarily assume the above simple function $f(t)$ with a peak at $1.1 \times 10^{13}$ N (Figure 9). We synthesize theoretical records at a receiver location $r = 67$ km, $\theta = \pi/2$ (on $x_1 - x_2$ plain) and $\varphi = 26°$ where

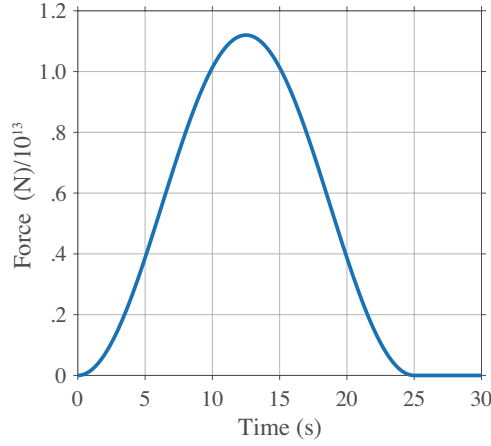Figure 9: Assumed time function $f(t)$ in the single force model with duration $25$ s and amplitude $1.1 \times 10^{13}$ N.

the seismogram for the events was recorded. We assume the P-wave velocity $\alpha = 5$ km/s and $t_p \simeq 13.4$ s.

Figure 10a shows the gravity change in the component $\delta g_3$ (note that $\delta g_1 = \delta g_2 = 0$ at that receiver). The signal attains $-0.8 \times 10^{-10}$ m/s$^2$ at $t = t_p$, approaches to $-2 \times 10^{-10}$ m/s$^2$ at $t = 22$ s, and returns to zero after $t_p + \tau_D$. Figure 10b shows the gravity-gradient changes in the components $\ddot{h}_{13}(t)$ and $\ddot{h}_{23}(t)$ (note that $\ddot{h}_{11} = \ddot{h}_{22} = \ddot{h}_{33} = \ddot{h}_{12} = 0$). The signal attains $3 \times 10^{-15}$ s$^{-2}$ at $t = t_p$, approaches to $5 \times 10^{-15}$ s$^{-2}$ at $t = 18$ s, and returns to zero. The gravity and gravity-gradient changes show different peak times because at the receiver the gravity change depends only on $I_2[F_3]$, whereas the gravity-gradient changes depend on both $I_2[F_3]$ and $F_3(t - r/\alpha)$.

Similarly to the double-couple case, we examine the relationship between the receiver distance and the prompt signal amplitude using $GI_2[f]/r^3 (= |GI_2[F_3]/r^3|)$ for the gravity change and $GI_2[f]/r^4 (= |GI_2[F_3]/r^4|)$ for the gravity-gradient changes (Figure 11). The prompt gravity change shows a peak at $r = 80$ km and its gradient just decays with $r$ corresponding to the initial rise of $f(t)$. The order of prompt signals are $10^{-10}$ m/s$^2$ and $10^{-15}$ s$^{-2}$. These theoretical prompt signals are too small to measure with existing instruments, so conventional television monitoring (with the speed of light) would be much more favorable for prompt detection of a volcanic eruption if it is visible on the surface.
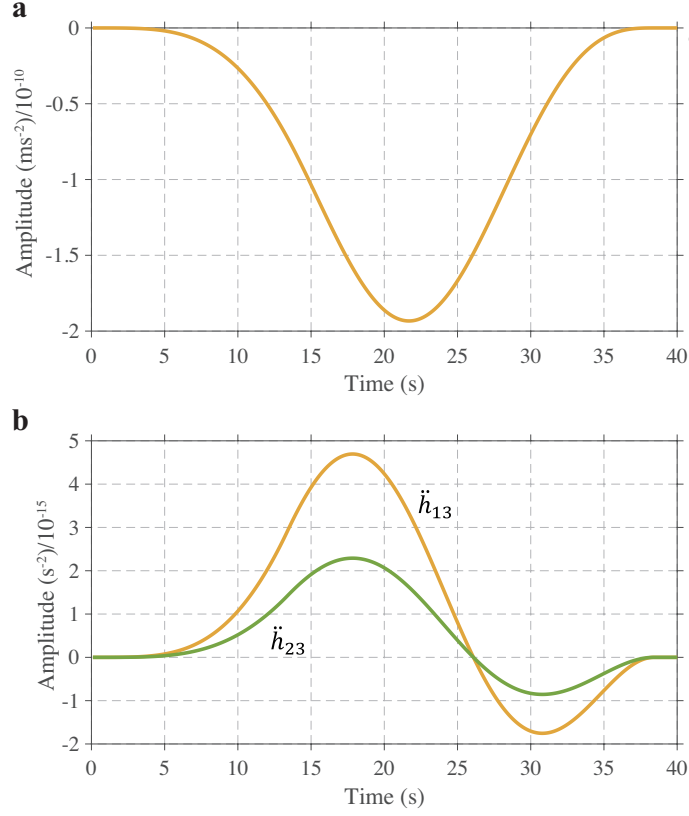
Figure 10: Synthesized gravity change and gravity-gradient changes at a receiver location $r = 67$ km, $\theta = 90°$, $\varphi = 26°$, where $t_p = 13.4$ s with the assumption $\alpha = 5$ km/s. (a) gravity change for the component $g_3(t)$. Note that $g_1 = g_2 = 0$ for the receiver. (b) gravity-gradient changes for the components $\ddot{h}_{13}(t)$ and $\ddot{h}_{23}(t)$. Note that $\ddot{h}_{11} = \ddot{h}_{22} = \ddot{h}_{33} = \ddot{h}_{12} = 0$.
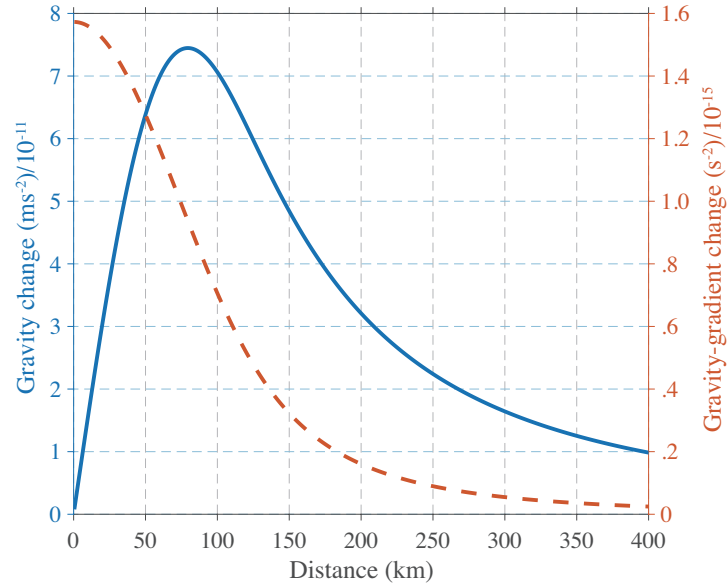


Figure 11: Plots of $GI_2[f]/r^3$ (solid line) and $GI_2[f]/r^4$ (dashed line) associated with the single force model of the 1980 St. Helens volcanic eruption. They show reference signal levels (without radiation coefficients) at receiver distances ($r$).

# 4 Discussion and Conclusions

We have presented analytical expressions for theoretical gravity and gravity-gradient changes associated with seismic radiations from a single force or a seismic moment tensor in an infinite homogeneous elastic medium. The formulae do not involve elastic coupling to the external static gravity and self-gravitating effects. For diverse seismic sources, except isotropic expansion, the equations functionally yield template waveforms for use in finding prompt gravity changes in time-series data recorded by state-of-the-art instruments.

As quantitative examples, we synthesized gravity and gravity-gradient changes for the 2011 Tohoku-Oki earthquake and the 1980 St. Helens eruption. The prompt gravity changes for the Mw 9.0 event were in the possible detection ranges, whereas the other signals were out of the detection ranges of existing instruments.

Prompt signals in gravity and gravity-gradient changes reflect the source-time function (moment function) and the source mechanism. Such signals, if practically measurable in multiple components and at multiple points, would contribute to constrain the source processes independently of widely used seismic-wave analyses. In addition, signal arrival times may lead to direct measurement of the propagation speed of gravity changes. These possibilities will be realistic challenges in future with the development of high-sensitivity instruments.

# References

[1] Aki, K. & Richards, P.G., 2002, Quantitative Seismology, 2nd. Ed., pp. 700, University Science Books, Susalito, California.

[2] Ando, M., Ishidoshiro, K., Yamamoto, K., Yagi, K., Kokuyama, W., Tsubono, K. & Takamori, A., 2010, Torsion-bar antenna for low-frequency gravitational-wave observations, *Phys. Rev. Lett.*, **105**, 161101, doi: 10.1103/PhysRevLett.105.161101

[3] Chu, R., Wei. S., Helmberger. D.V., Zhan, Z., Zhu, L., & Kanamori, H., 2011, Initiation of the great Mw 9.0 Tohoku-Oki earthquake, *Earth Planet. Sci. Lett.*, **308**, 277-283, doi:10.1016/j.epsl.2011.06.031

[4] Harms, J., Ampuero, J.-P., Barsuglia, M., Chassande-Mottin, E., Montagner, J.-P., Somala, S. N. & Whiting, B. F., 2015, Transient gravity perturbations induced by earthquake rupture, *Geophys. J. Int.*, **201**, 1416-1425, doi: 10.1093/gji/ggv090

[5] Harms, J., 2016, Transient gravity perturbations from a double-couple in a homogeneous half-space, *Geophys. J. Int.*, **205**, 1153-1164, doi: 10.1093/gji/ggw076

[6] Ichihara, M., Kusakabe, T., Kame, N. & Kumagai, H., 2016, On volume-source representations based on the representation theorem, *Earth Planets Space*, **68:14**, doi:10.1186/s40623-016-0387-3

[7] Imanishi, Y., Sato, T., Higashi, T., Sun, W. & Okubo, S., 2004, A network of superconducting gravimeters detects submicrogal coseismic gravity changes, *Science*, **306**, 476-478.

[8] Kanamori, K., & Given, J.W., 1983, Lamb pulse observed in nature, *J. Geophys. Res.*, **10**, 373-376.

[9] Kennett, B. L. N., 1975, Theoretical seismogram calculation for laterally varying crustal structures, **42**, 579-589.

[10] Kumagai, H., Pulido, N., Fukuyama, E. & Aoi, S., 2012, Strong localized asperity of the 2011 Tohoku-Oki earthquake, Japan, *Earth Planets Space*, **64**, 649-654, doi:10.5047/eps.2012.01.004

[11] Kumagai, H., Maeda, Y., Ichihara, M., Kame, N. & Kusakabe, T., 2014, Seismic moment and volume change of a spherical source, *Earth Planets Space*, **66:7**, doi:10.1186/1880-5981-66-7

[12] Montagner, J-P., Juhel, K., Barsuglia, M., Ampuero, J-P., Chassande-Mottin, E., Harms, J., Whiting, B., Bernard, P., Clévédé, E., & Lognonné, P., 2016,

Prompt gravity signal induced by the 2011 Tohoku-Oki earthquake, *Nature Comm.*, doi:10.1038/ncomms13349

[13] Okubo, S., 1991, Potential and gravity changes raised by point dislocations, *Geophys. J. Int.*, **105 (3)**, 573-586.

[14] Sato, Y., Usami, T. & Landisman, M., 1965, Theoretical seismograms of spheroidal type on the surface of a heterogeneous spherical earth, *Bull. Earth. Res. Inst.*, **43**, 641-660.

[15] Sato, Y., Usami, T. & Landisman, M., 1968, Theoretical seismograms of torsional disturbances excited at a focus within a heterogeneous spherical earth - Case of a Gutenberg-Bullen A ' earth model, *Bull. Seism. Soc. Am.*, **58**, 133-170.

[16] Shoda, A., Ando, M., Ishidoshiro, K., Okada,K., Kokuyama,W., Aso, Y. & Tsubono, K., 2014, Search for a stochastic gravitational-wave background using a pair of torsion-bar antennas, *Phys. Rev. Lett. D*, **89**, DOI: 10.1103/PhysRevD.89.027101

[17] Tanaka, Y., Okubo, S., Machida, M., Kimura, I. & Kosuge, T., 2001, First detection of absolute gravity change caused by earthquake, *Geophys. Res. Lett.*, **28**, 2979-2981.

[18] Wei, S., Graves, R., Helmberger, D., Avouac, J.-P. & Jiang, J., 2012, Sources of shaking and flooding during the Tohoku-Oki earthquake: A mixture of rupture styles, *Earth Planet. Sci. Lett.*, **333**, 91-100.

# Chapter 3

# Search for prompt gravity signals in data and its interpretation based on the principle of gravimetry

## SUMMARY

Dynamic earthquake rupture causes density changes of the medium and, in theory, induces prompt gravity perturbations at all distances before the arrival of seismic waves. Detection of the prompt gravity signal before the seismic one is a challenge in seismology. In this study, we searched high sampling-rate gravimetric data for such prompt gravity changes induced by the 2011 Tohoku-Oki earthquake using a band-pass filtering method. However, no significant changes predicted by a theoretical model were identified even though the data had sufficient signal-to-noise ratios. We also analyzed stacked broadband seismograph and tiltmeter array data and again could not detect the expected changes. To interpret the absence of signals in the data, we investigated the self-gravity effect on the measurement of gravitational acceleration, which has been ignored in the existing theory. For this purpose, we calculated the displacement of the observation station before $P$ wave arrival and showed that each point in the medium moves at an acceleration identical to the applied gravity change. This means that the above gravity sensors do not have sensitivity in principle to the prompt gravity change because of the opposite inertial force. Despite the negative observability in acceleration, there remains possibility of detection in terms of its spatial gradients. The analytical

expression for the theoretical gravity gradients from a general seismic source we derived in Chapter 2 is useful toward future research.

# 1 Introduction

Seismic waves radiated from an earthquake accompany density perturbations, which give rise to the transient gravity perturbations everywhere, even outside the seismic wave front. The possibility of earthquake-induced prompt gravity signals has been studied by *Harms et al.* [2015] and *Harms* [2016]. Such signals, if practically measurable, can be the fastest method to detect earthquake occurrences, which could help issuing early warnings for large earthquakes and tsunamis [*Harms et al.*, 2015]. After the P-wave arrival, the observation sites start to undergo seismic shaking, and a small change of the gravity field cannot be measured because of the overwhelming effect of the ground acceleration.

Recently, *Montagner et al.* [2016] searched for the signal induced by the 2011 Mw 9.0 Tohoku-Oki earthquake in data recorded by a superconducting gravimeter at Kamioka and five nearby F-net broadband seismometers in Japan. They could not find any signal with an amplitude that obviously stood above the background microseism noise. Then, they defined a 'reduced gravity signal *A*' of the segment before *P* wave arrival, which means the time-averaged noise level, and compared it with those of the other background segments where no event occurred. As the result of a statistical procedure, they found that the 'reduced gravity signal *A*' of the segment before *P* wave arrival was bigger than those of the other segments with a statistical significance higher than 99% and claimed the presence of a prompt gravity signal from the event. However,

the synthetic gravity waveforms predicted by a theory were not used in their analysis, so definite detection of the signal has not been done yet.

In section 2, we investigated high sampling-rate data from two superconducting gravimeters operated at Kamioka and Matsushiro. We also examined data from the F-net broadband seismometer and the Hi-net tiltmeter arrays. In contrast to the statistical approach of *Montagner et al.* [2016], we took a deterministic approach, computing expected waveforms based on the theory of *Harms et al.* [2015] (Figure 12) and identifying them definitely in the observed time-series data. To reduce the noise level, we adopted a conventional band-pass filtering method, and for the array data we also applied a station-stacking method.

As a result, no significant prompt signals exceeding the noise amplitude were identified in the recordings. We constrained the upper limits of recorded signals, which were smaller than the theoretical predictions. This raises the inconsistency between the observed data and the simplified theory currently used.

In section 3, we investigated the effect of self-gravity deformation of the Earth on the measurements of gravitational acceleration to interpret this absence of gravity signals. This effect has been neglected in the current simplified model. In the first step, we solved the elastodynamic equation of motion loaded by the prompt gravity changes and obtained the analytical solution of the resultant displacement accelerations in an elastic full space. In the second step, we developed an observation model that incorporated the motion of observation ground induced by self-gravity.

We verified that the inertial force arising from the ground motion induced by self-gravity completely cancels out the prompt gravity force acting on a sensor mass in

a gravimeter, which inevitably leads to a null signal in an accelerogram. Our theory discloses the negative observability of earthquake-induced prompt gravity changes using acceleration sensors.

In section 4, we argued the intrinsic nature of gravity-induced elastic deformation. We showed that instantaneous gravity changes, not limited to those from earthquakes, necessarily accompany temporary free fall of the medium until the seismic waves arrive. A gravimeter acts as if it were installed in an Einstein's elevator, and loses its sensitivity to gravitational acceleration. However, detection in terms of the gravity gradients remains possible. The analytical expression of theoretical gravity-gradient changes from a general seismic point source represented by a moment tensor we derived in Chapter 2 can be used as template waveforms in time-series analysis.

## 2  Data analysis

### 2.1  Theoretical accelerogram

We use the term 'theoretical accelerograms' to denote the theoretical gravity waveforms we derived in Chapter 2: the expected time-varying perturbation of the gravitational acceleration from an earthquake at a receiver location. It works as a template waveform in time-series data analysis.

For the following data analyses, we use equation (21) in Chapter 2 and synthesize theoretical accelerograms of the 2011 Tohoku-Oki earthquake. Figure 12a shows the vertical component of the theoretical gravity change at Kamioka, where a superconducting gravimeter had been deployed. We set the event origin time $t_{eq}$ and
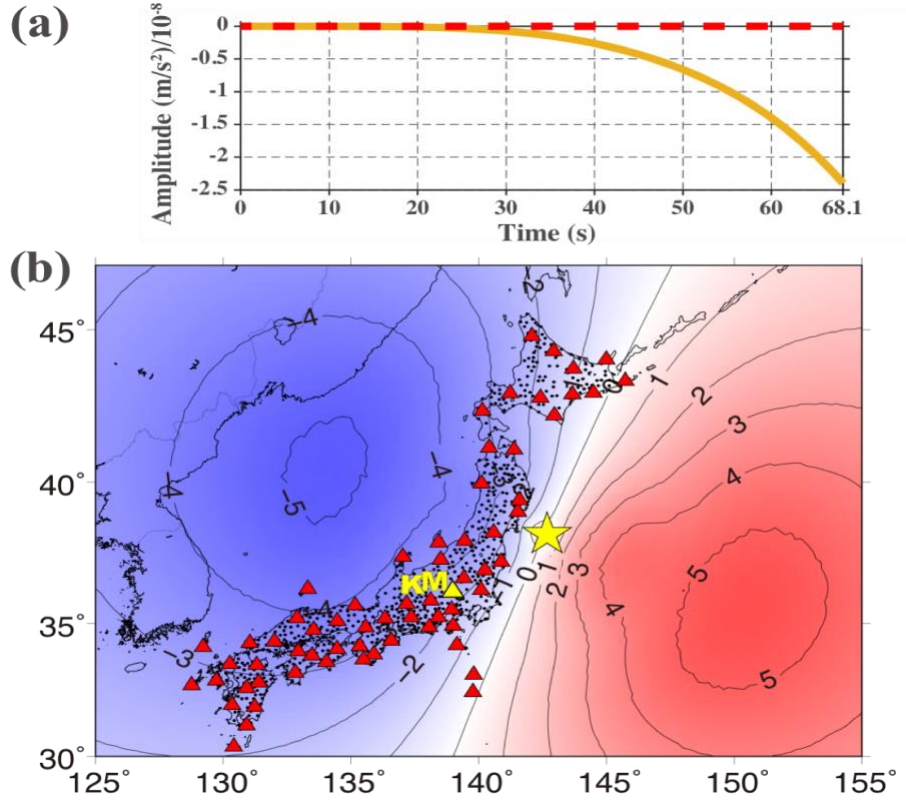
Figure 12. (a) The solid and dashed lines denote the theoretical accelerograms (vertical component with upward positive) of the 2011 Tohoku-Oki earthquake synthesized for the Kamioka Observatory predicted by *Harms et al.* [2015] and by our model incorporated with the self-gravity effect (see section 3), respectively. Time 0 is set to the event origin time $t_{eq}$. The distance between the hypocenter and Kamioka is 515 km, and the *P* wave arrival time on the gravimetric record is 05:47:32.4 UTC (68.1 s after $t_{eq}$). (b) Distribution of prompt gravity changes (vertical component with upward positive) immediately before *P* wave arrival at each location. The star, K, M, yellow triangle, red triangle, and small dot symbols indicate the epicenter, the Kamioka Observatory, the Matsushiro Observatory, the Onishi F-net station, 70 other F-net stations, and 706 tiltmeter stations, respectively. The contour lines are drawn at every $10^{-8}$ m/s$^2$.

location to $05\!:\!46\!:\!24.3$ UTC and 38.19N, 142.68E, 21km (depth), respectively, following *Chu et al.* [2011]. The $P$ wave arrival time $t_P$ is visually picked in each data record. For example, on the gravimetric record, $t_P = 05\!:\!47\!:\!32.4$ UTC (68.1 s after $t_{eq}$) at Kamioka. During the prompt period $t_{eq} < t < t_P$, the theoretical accelerogram monotonically decreases and reaches $-2.4 \times 10^{-8}$ m/s$^2$ at $t_P$.

## 2.2 Searches for predicted waveforms in data

Based on the synthesized accelerograms, we searched for prompt gravity signals induced by the 2011 Mw 9.0 event in data recorded in Japan. We analyzed three different types of high sampling-rate data: gravity data from two superconducting gravimeters (SG), ground velocity data from the F-net seismographic array (F-net), and horizontal acceleration data from the Hi-net tiltmeter array (Hi-net). All 71 F-net stations are equipped with an STS-1 or STS-2 type broadband seismometer. A two-component borehole tiltmeter is installed at 706 Hi-net stations. These instruments are listed in Table 1, and the locations of the stations are shown in Figure 12b.

Table 1. List of observation instruments.

| Instrument | Channels used | Output used |
|---|---|---|
| Superconducting gravimeter | 2 (Kamioka and Matsushiro) | Vertical gravity acceleration [m/s$^2$] |
| Broadband seismometer | 70 out of 71 (F-net) | Vertical ground velocity [m/s] converted to acceleration |
| Tiltmeter | 549 out of 1412 (Hi-net) | Ground tilt [rad] converted to horizontal acceleration |

## 2.2.1 Superconducting gravimeters

We used the SG data recorded at a 40 Hz sampling (GWR5 channel) [*Imanishi*, 2001]. Figure 13 shows the comparison of the original data with the theoretical accelerogram at Kamioka. The sensor response was included in the theoretical accelerogram. Background microseism dominated, with an amplitude of $10 \times 10^{-8}$ m/$s^2$, which is a few times larger than the expected gravity change, so no signal was identified.

To reduce the microseism noise, we applied frequency filtering. Figure 14 is the noise power spectrum of a 40-min time window recorded between 05:00 and 05:40 UTC. In contrast to the 1 Hz sampling data (GGP1 channel) with a 0.061 Hz anti-
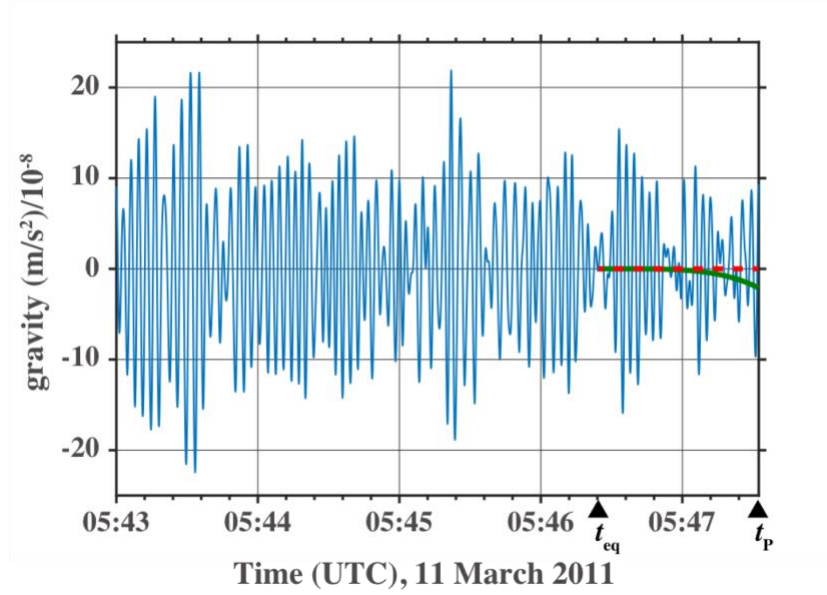


Figure 13. The original superconducting gravimeter (SG) data at Kamioka with zero direct current offset (40 Hz sampling rate) and the theoretical accelerograms convoluted with the SG instrumental response (Solid: SG data, Thick solid: *Harms et al.* [2015], Dashed: our model (see section 3)).

aliasing filter used in the analysis of *Montagner et al.* [2016], our 40 Hz sampling data contain signal power in the frequency range higher than 0.061 Hz. However, the spectrum shows relatively large noise power higher than 0.05 Hz, and we applied a band-pass filter between 0.001 Hz and 0.03 Hz (5th-order 0.001 Hz high-pass and 0.03 Hz low-pass causal Butterworth filters) for both the original data and the synthetic accelerogram. The lower frequency of 0.001 Hz is set to remove the long period tidal variation.
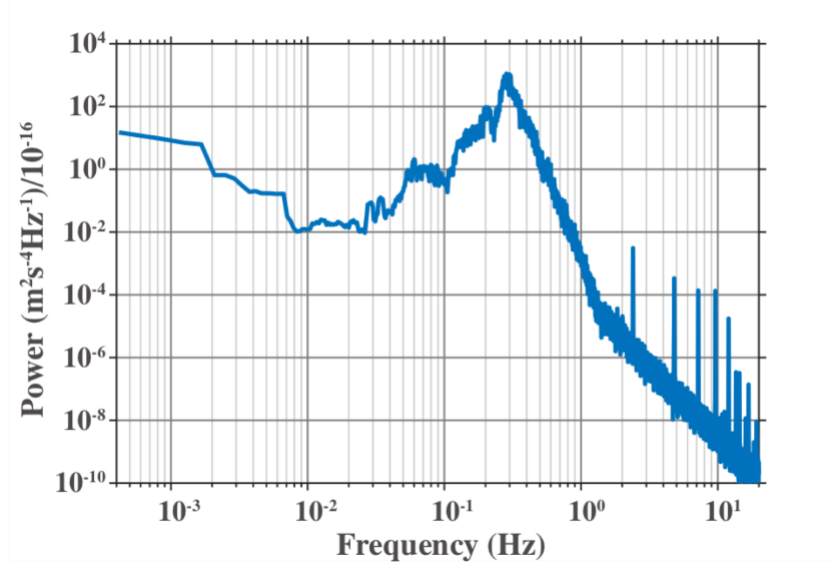


Figure 14. Noise power spectrum of 40-min time window between 05:00 and 05:40 UTC from the Kamioka superconducting gravimeter data before the 2011 Tohoku-Oki event.
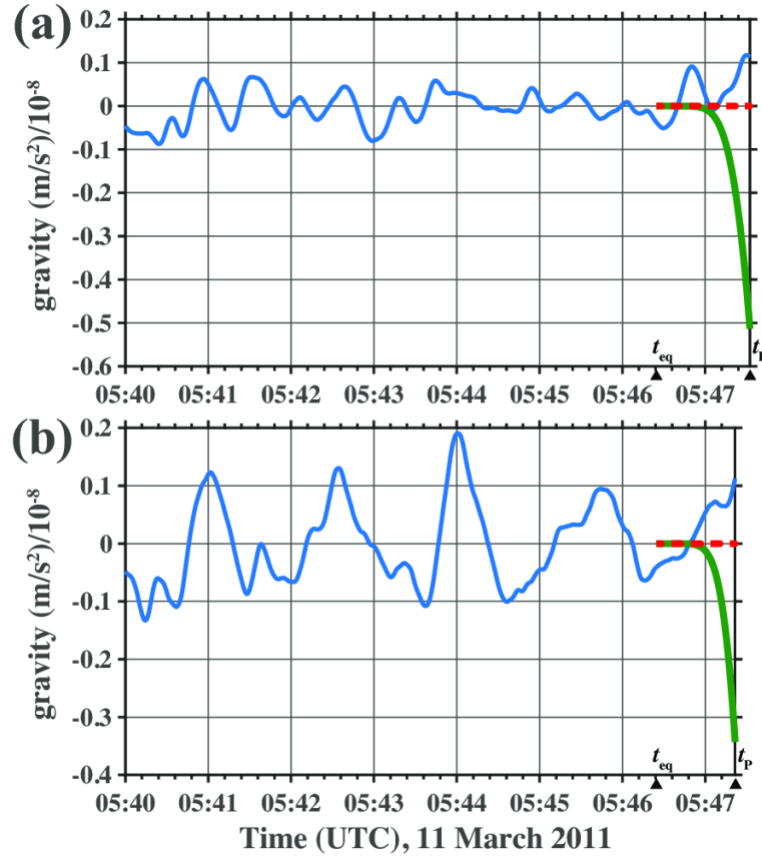
Figure 15. The 0.001–0.03 Hz band-pass-filtered superconducting gravimeter (SG) data and the theoretical accelerograms (Solid: SG data, Thick solid: Harms et al. [2015], Dashed: our model (see section 3)). (a) Plot for Kamioka. (b) Plot for Matsushiro.

Figure 15a shows the comparison between the data and the theoretical accelerogram after the filtering. The noise in the data was significantly reduced, whereas the amplitude of the theoretical signal was less reduced. It seems that no significant earthquake-induced gravity signal prior to the P wave arrival exists in the data.

For quantitative evaluation, we define the theoretical signal level $A_S$ and microseism noise level $A_N$ as follows:

$$A_S = |\delta g(t_P)|, \tag{29}$$

$$A_N = \sqrt{\frac{1}{t_2 - t_1} \int_{t_1}^{t_2} [x(t) - \mu]^2 dt}, \tag{30}$$

where $\delta g(t)$ is the theoretical accelerogram, $x(t)$ is the observed data, $t_1 = 05{:}40$ UTC, $t_2 = 05{:}46.405$ UTC $\left(= t_{eq}\right)$, and $\mu = \frac{1}{t_2 - t_1} \int_{t_1}^{t_2} x(t) dt$. For the Kamioka data, $A_N$ was reduced from $7 \times 10^{-8}$ m/s$^2$ to $0.04 \times 10^{-8}$ m/s$^2$ after the filtering, whereas the signal level $A_S$ retained an amplitude as large as $0.5 \times 10^{-8}$ m/s$^2$. The S/N ratio $(A_S/A_N)$ was greater than ten which is large enough to identify the signal.

Figure 15b shows a comparison between the data and the theoretical accelerogram after the same filtering at Matsushiro (436 km from the hypocenter and $t_P = t_{eq} + 57.3$ s). $A_N$ was reduced from $8 \times 10^{-8}$ m/s$^2$ to $0.07 \times 10^{-8}$ m/s$^2$ and $A_S$ retained an amplitude of $0.3 \times 10^{-8}$ m/s$^2$ after the filtering. Again, we did not recognize the predicted waveform even though the S/N ratio reached about four. We conclude that the expected signals were not recorded in the SG data with significant intensity.

## 2.2.2 F-net broadband seismometers

A seismometer is based on an inertial sensor and measures the mass position relative to the ground. The prompt gravity change would move the mass, which is expected to be recorded by the instrument. Note that vertical sensors output down signals for upward gravity changes.

Frequency responses of the F-net seismometers to velocity are flat between 0.003 and 10 Hz. Consequently, we did not apply the sensor frequency responses to the

theoretical accelerograms and converted the velocity data into acceleration through single derivation.

In the vertical component of the F-net data, the typical value of $A_N$ was $100 \times 10^{-8}$ m/s$^2$ ($34 \times 10^{-8}$ m/s$^2$ at the lowest). They were tens to a hundred times larger than $A_S$, and we only saw microseismic ground oscillation before filtering. To reduce the noise, we again applied the same filters. Figure 16 shows an example recorded at Onishi. After the filtering, the microseism noise was successfully reduced to as low as $0.02 \times 10^{-8}$ m/s$^2$, whereas the theoretical signal stayed as large as $0.2 \times 10^{-8}$ m/s$^2$, thus the S/N ratio was greater than ten. We repeated the same analysis for all available data from 70 out of the 71 stations, omitting one because of poor recording quality. The S/N ratios after the filtering ranged from 0.1 to 60. At any station, we could not find any signal comparable to the predicted one even though 43 stations indicated S/N ratios larger than ten. We show all the 70 filtered waveforms in Supplement.
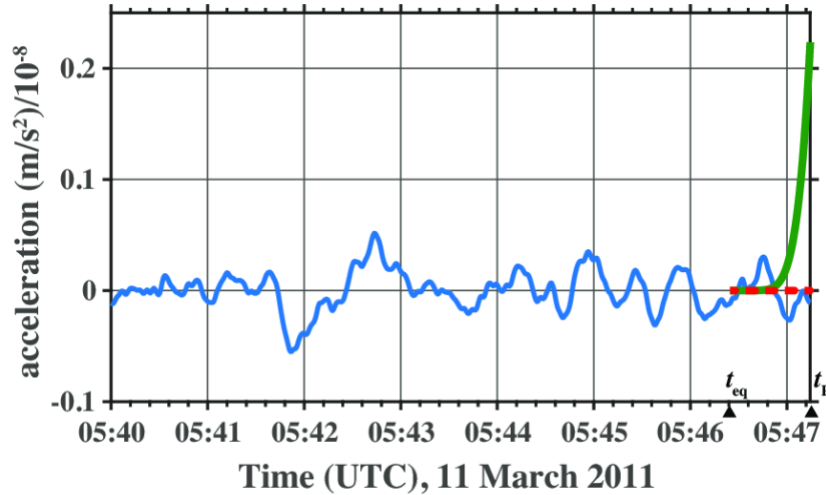


Figure 16. The F-net data and the theoretical accelerograms at Onishi with 0.001–0.03 Hz band-pass filtering (Solid: F-net data, Thick solid: Harms et al. [2015], Dashed: our model (see section 3)).

Next, a multi-station signal-stacking method was applied to enhance signals of interest relative to noise. After the band-pass filtering, we stacked the time series aligned with $t_P$ at each station (Figure 17) with polarity reversal correction, i.e., multiplying each time series by one or minus one based on the sign of the theoretical gravity change. The stacked F-net trace for the 43 stations with S/N ratios larger than ten was compared with the stacked theoretical accelerograms (Figure 18a). As expected, the noise of the stacked trace decreased, and the S/N ratio increased to 100 ($A_N$ calculated for 10 min before the reference time ($t_1 = -10$ min, $t_2 = 0$) was $0.004 \times 10^{-8}$ m/s$^2$, whereas $A_S$ stayed at $0.5 \times 10^{-8}$ m/s$^2$). Even though the stacked trace showed a large S/N ratio, we did not see any significant signal as predicted by the theoretical model. It is worth noticing that the stacked trace shows a very slight negative trend beyond the noise level toward the P wave arrival, which is discussed in Section 4.
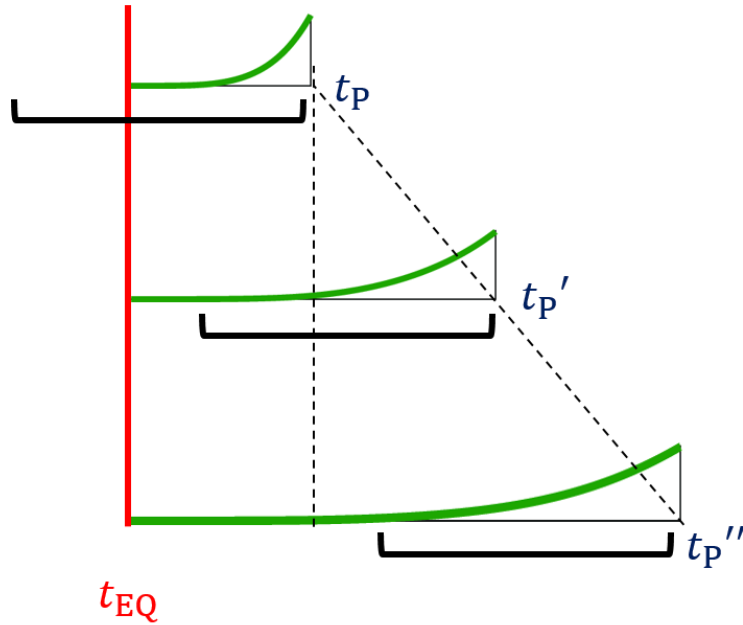


Figure 17. How to stack the waveforms at the P-wave arrival time of each station.
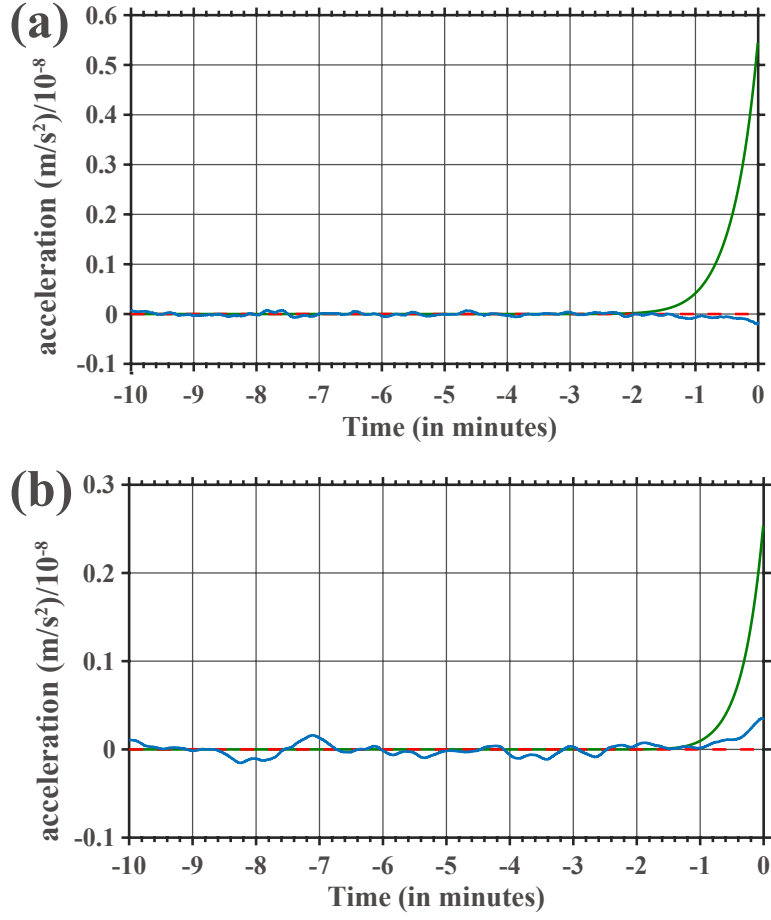
Figure 18. **(a)** Stacked waveform of the filtered F-net data and the theoretical accelerograms (Solid: F-net data, Thick solid: *Harms et al.* [2015], Dashed: our model (see section 3)). Time 0 is set to the stacking reference time $t_P$. **(b)** Stacked waveform of the filtered Hi-net tiltmeter data and the theoretical accelerograms (Solid: Hi-net data, Thick solid: *Harms et al.* [2015], Dashed: our model (see section 3)). The difference of stacked theoretical accelerograms between F-net and Hi-net is due to the distribution of the stations used for stacking.

### 2.2.3 Hi-net tiltmeters

We analyzed the data recorded by the Hi-net tiltmeters, which work as horizontal seismometers. For our analysis, tilt data were converted into horizontal acceleration. Because the sensor response is not open, we could not apply it to the theoretical accelerograms; however, tiltmeter records have been used as seismic records by comparing them with nearby broadband seismic records (e.g., within a bandwidth of 0.02–0.16 Hz) [*Tonegawa et al.*, 2006]. Because tiltmeters are designed to respond to static changes, recordings will also be reliable below 0.02 Hz.

Hi-net tiltmeter data were generally noisy compared to F-net data. The typical value of $A_N$ for the 40-min duration was $200 \times 10^{-8}$ m/s$^2$. After applying the same filters, we picked up and stacked 549 traces of data out of 1412 traces (two horizontal components from each station). These traces were chosen following the criterion of S/N ratio larger than unity. We compared the stacked tiltmeter trace to the stacked theoretical accelerograms (Figure 18b). The noise in the stacked trace was as low as $0.008 \times 10^{-8}$ m/s$^2$, whereas $A_S$ stayed at $0.25 \times 10^{-8}$ m/s$^2$, which resulted in an S/N ratio of 30. Again, the predicted signal cannot be identified, but the stacked trace shows a positive trend beyond the noise level toward the P wave arrival, which is also discussed in Section 4..

### 2.2.4 Upper limit of gravity signal

Our analyses of the SG, F-net, and Hi-net data yielded upper limits of the gravity signals. The 95% confidence level upper limit is given by $2\sigma$, where $\sigma$ is the standard deviation of time-series data. In our analyses, $2\sigma$ is equal to $2A_N$, so the upper limits

were $0.1 \times 10^{-8}$ m/s$^2$ at Kamioka and Matsushiro, and $0.04 \times 10^{-8}$ m/s$^2$ at Onishi. After stacking, the reduced noise levels were $0.01 \times 10^{-8}$ m/s$^2$ for the F-net data and $0.06 \times 10^{-8}$ m/s$^2$ for the Hi-net data. They were all smaller than the predicted values. Our analyses confirmed the absence of the predicted gravity signals in the observed data, which raises inconsistency between the simplified theory and the data.

# 3 Interpretation of absence of prompt signals based on the principle of gravimetry

Here, we investigate the self-gravity effect to interpret the absence of prompt gravity signals in the data. This effect was neglected in the theoretical modeling of *Harms et al.* [2015], but it may induce ground motion before *P* wave arrival and affect gravitational acceleration measurements via an inertial force to the sensor mass [*Heaton,* 2017]. For this purpose, we derive the analytical expression of the elastic deformation induced by the prompt gravity changes in an elastic full space. Then, we develop an observation model where we incorporate the effect of the ground motion.

*Harms et al.* [2015] employed simplified Earth structure and earthquake source models and simplified laws of physics for brevity: (i) a point earthquake source, (ii) an infinite homogeneous medium, (iii) no time-constant background gravity field that would affect deformation under gravity, and (iv) no mutual interaction between the induced gravity change and the medium mass. We suspect that these simplified assumptions might have artificially enhanced the theoretical signals so that they exceeded the noise level and would be easily detected as plotted in Figures 15, 16, and 18.

## 3.1 Elastic deformation induced by prompt gravity changes

The simplified model of *Harms et al.* [2015] considered only the prompt gravity changes induced by pure elastic deformation, and formulated in the time-domain an explicit expression of the prompt gravity changes induced by an earthquake in a homogeneous full space without assuming the self-gravity effect (Figure 19). Here by extending *Harms et al.* [2015], we obtain the analytical expression of elastic
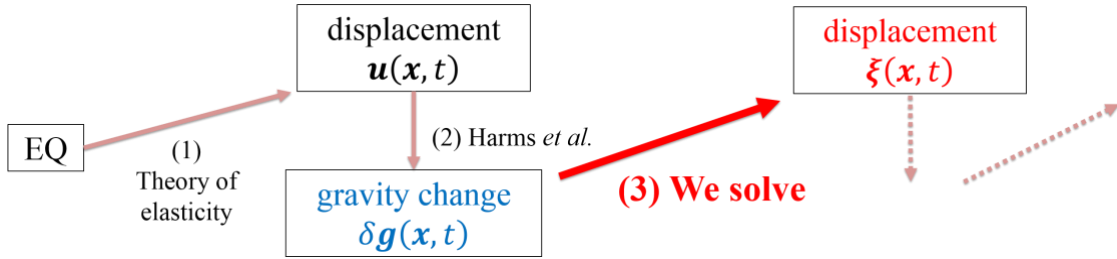


Figure 19. Flowchart of the interaction between the displacement of the medium and the gravity change.

deformation in the time-domain induced by the prompt gravity changes in a homogeneous full space. This solution represents the first order perturbation of elastic deformation induced by the first order perturbation of gravity.

The formulation starts with the equation of motion of an infinite isotropic homogeneous elastic medium [e.g., *Aki and Richards*, 2002]:

$$\rho\ddot{\boldsymbol{\xi}}(\boldsymbol{x},t) = (\lambda + 2\mu)\nabla(\nabla \cdot \boldsymbol{\xi}(\boldsymbol{x},t)) - \mu\nabla \times (\nabla \times \boldsymbol{\xi}(\boldsymbol{x},t)) + \boldsymbol{f}(\boldsymbol{x},t), \qquad (31)$$

where $\boldsymbol{\xi}(\boldsymbol{x},t)$ is the displacement field, $\ddot{\boldsymbol{\xi}}$ is the second derivative of $\boldsymbol{\xi}$ with respect to time, $\lambda$ and $\mu$ are the *Lame* constants and $\boldsymbol{f}(\boldsymbol{x},t)$ is the body force distribution. We seek the solution $\boldsymbol{\xi}(\boldsymbol{x},t)$ for a given body force $\boldsymbol{f}(\boldsymbol{x},t) = \rho\delta\boldsymbol{g}(\boldsymbol{x},t)$, which represents the elastodynamic deformation induced by the prompt gravity changes. The mathematical

procedure of deriving the solution is summarized in appendix A. Interestingly, the solution for the prompt period $0 < t < t_P = r/\alpha$ is quite simple:

$$\ddot{\xi}(x,t) = \delta g(x,t). \tag{32}$$

This solution shows that the ground acceleration at a receiver is identical to the prompt gravity change acting there.

## 3.2 Negative observability of earthquake-induced prompt gravity in acceleration

We develop an observation model that includes the effect of self-gravity deformation on the measurement of gravitational acceleration. Figure 20 shows the principle of gravimetry. A gravimeter based on an inertial sensor is essentially a mass suspended by a spring. What the instrument can measure is not the gravity $Mg(t)$ acting on the sensor
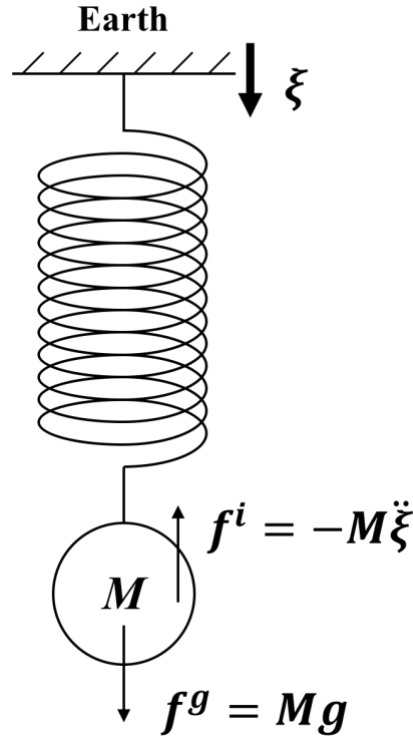


Figure 20. The principle of relative gravity measurement.

mass $M$, but the relative motion of the mass to the instrument. Therefore, the output $s(t)$ is the difference between the gravity acceleration $g(t)$ and the acceleration of the attached ground $\ddot{\xi}(t)$:

$$s(t) = g(t) - \ddot{\xi}(t). \tag{33}$$

This can be expressed as follows: both gravitational force $Mg(t)$ and inertial force $-M\ddot{\xi}(t)$ act on the mass, and the sensor feels only the resultant force.

At any observation location, the ground acceleration $\ddot{\boldsymbol{\xi}}(\boldsymbol{x}, t)$ during the prompt period is equal to the gravity change $\delta \boldsymbol{g}(\boldsymbol{x}, t)$ (equation 32). From equation 33, the predicted sensor output is

$$s(t) = g(t) - \ddot{\xi}(t) = \big(g_0 + \delta g(t)\big) - \delta g(t) = g_0 : \text{const.}, \tag{34}$$

where $g_0$ is the reference gravity before the earthquake. The prompt gravity signal is canceled out by the ground motion induced by the self-gravity effect: a gravimeter loses its sensitivity during the prompt period. Our model shows the negative observability of earthquake-induced prompt signals in the acceleration measurement. Absolute gravimeters are not the exception because they also depend on the relative motion of the test mass to the ground.

Theoretical accelerograms predicted by our model (i.e., zero amplitude) are shown as dashed lines in Figures 12a, 13, 15, 16, and 18. Clearly, the observed data are more consistent with our model, i.e., null signals in accelerograms, than with the model proposed by *Harms et al.* [2015].

# 4. Discussion

## 4.1  Inevitable free fall of a gravimeter in response to instantaneous gravity change

We have shown the elastic response to the prompt gravity: the resultant ground acceleration is parallel to the applied gravity change (equation 32). It gives us an insight into the intrinsic nature of an elastic solid in response to an instantaneously applied gravity change. Namely, each point of the medium falls freely as if it were an isolated mass in space when inhomogeneous gravity change $\delta g(x, t)$ is instantaneously applied at $t = 0$.
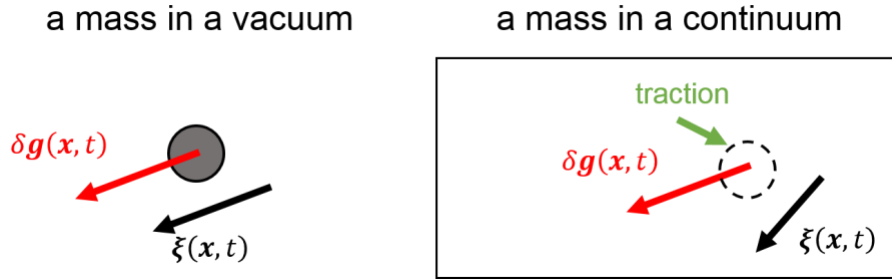


Figure 21. Schematic illustration of the motion of a mass in a vacuum or a continuum.

In a continuum, such free-fall motion is counterintuitive; a volume of interest is never able to move like an isolated mass because of the surrounding medium, i.e., a mass buried in the ground never falls freely. The surrounding medium does affect the volume via adjoining surfaces, i.e., traction, which should prevent the volume from free falling (Figure 21).

To repel such erroneous intuition, we return to the equation of motion (equation 31). The first two terms on the right-hand side represent the local forces due to traction and the last term represents the remote body force due to the gravity change. If a gravity
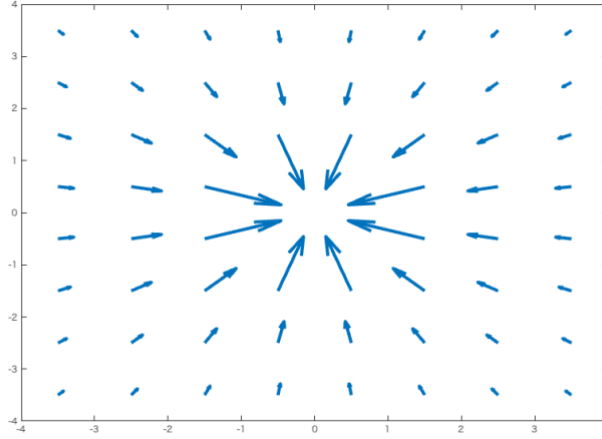
Figure 22. The gravity field induced by a point mass.

change $\delta\boldsymbol{g}(\boldsymbol{x}, t)$ instantaneously appears at $t = 0$, it is shown, as below, that the displacement field $\ddot{\boldsymbol{\xi}}(\boldsymbol{x}, t) = \delta\boldsymbol{g}(\boldsymbol{x}, t)$ surely satisfies the equation of motion.

Suppose single mass $M$ emerges at $\boldsymbol{x} = \boldsymbol{0}$ and $t = 0$. The gravity field induced by this mass is $\delta\boldsymbol{g}(\boldsymbol{x}, t) = -GM\frac{\boldsymbol{x}}{r^3}$ $(t \geq 0)$, where $r = |\boldsymbol{x}|$, which decays with $r^2$ (Figure 22). Its rotation is zero everywhere and its divergence is zero except $\boldsymbol{x} = \boldsymbol{0}$ where the mass emerges. Here, we assume that the solution of displacement $\boldsymbol{\xi}(\boldsymbol{x}, t)$ satisfies $\ddot{\boldsymbol{\xi}}(\boldsymbol{x}, t) = \delta\boldsymbol{g}(\boldsymbol{x}, t)$. In the framework of infinitesimal deformation, the displacement $\boldsymbol{\xi}$ and the gravity $\delta\boldsymbol{g}$ have a spatially identical distribution: $\boldsymbol{\xi} = \frac{1}{2}\delta\boldsymbol{g}t^2$. This equation leads to $\boldsymbol{\nabla} \times \boldsymbol{\xi} = \boldsymbol{0}$ and $\boldsymbol{\nabla} \cdot \boldsymbol{\xi} = 0$, except when $\boldsymbol{x} = \boldsymbol{0}$, which means that the traction terms of the equation of motion are equal to zero. Thus, the solution $\ddot{\boldsymbol{\xi}}(\boldsymbol{x}, t) = \delta\boldsymbol{g}(\boldsymbol{x}, t)$ surely satisfies the equation of motion except where the mass emerges. For the emergence of spatially distributed mass, i.e., density changes (Figure 23), the solution of displacement is a mere superposition of that for single mass, so $\ddot{\boldsymbol{\xi}}(\boldsymbol{x}, t) = \delta\boldsymbol{g}(\boldsymbol{x}, t)$ also holds except for the region where the density changes occur. In

the case of earthquake-induced gravity, this condition corresponds to that the *P* waves have not yet arrived.

This free-fall deformation of the ground is not limited to earthquake-induced gravity change, but the intrinsic nature of the elastic response to arbitrary gravity change. This is exactly an Einstein's elevator temporarily appearing on Earth, in which a person does not feel the gravitational acceleration because of the opposite inertial force. This phenomenon has been unnoticed in the classical frequency-domain normal mode theory.

## 4.2  Higher interactions of self-gravity

We have considered only the first order perturbation in gravity and deformation. Here,
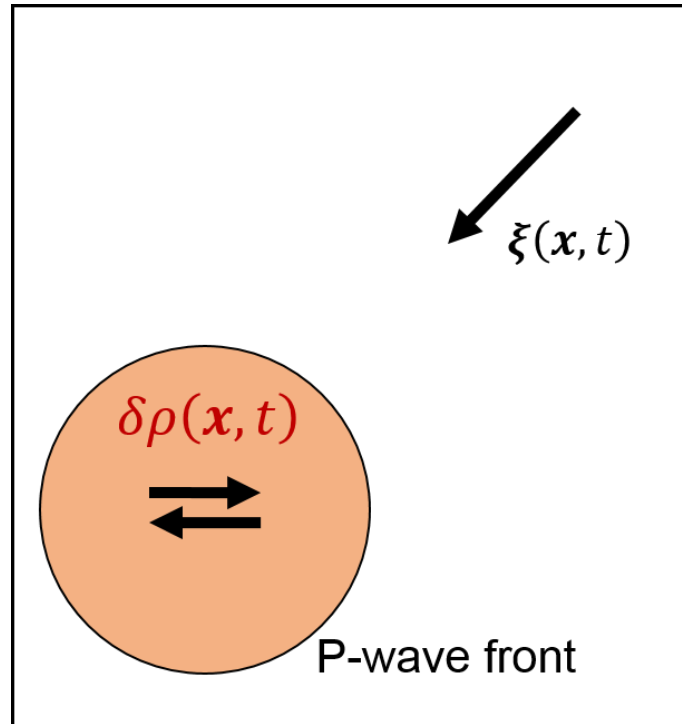


Figure 23. A seismically causal region where density perturbation occurs, and a seismically non-causal region where prompt gravity change occurs without density perturbation.

we investigate the effect of higher interactions that may be also important in the measurement of gravitational acceleration. We have shown that the first order perturbation in deformation $\xi(x,t)$ induced by the first order perturbation in gravity $\delta g(x,t)$ has the form $\ddot{\xi}(x,t) = \delta g(x,t)\,(0 < t < t_P)$. Outside the $P$ wave front, because the divergence of the first order perturbation in deformation is zero, the resultant density perturbation is also zero from equation 2. As a result, the density perturbations occur only inside the $P$ wave front, so in the acceleration measurement the higher order perturbations in gravity are canceled out by the resultant higher order perturbations in deformation as $\delta g(x,t)$ is canceled out by $\xi(x,t)$. This is why the first interaction is critical and the higher order interactions are negligible in the gravitational acceleration measurement.

## 4.3 Two types of self-gravity effect

In the normal mode theory, there are two types of Newtonian interactions between density and gravity: (i) between the background gravity field and the elastic deformation, (ii) between the gravity perturbation and the initial elastic mass. Both gravity forces are called self-gravity. We investigated the perturbation in deformation $\xi(x,t)$ induced by the prompt gravity perturbation $\delta g(x,t)$ in section 3.1, which corresponds to the type (ii) self-gravity effect. The type (i) effect occurs only where the deformation $u(x,t)$ exists, i.e., where $P$ waves have arrived. Before the arrival of $P$ waves, we can ignore the type (i) self-gravity effect on deformation.

## 4.4 The effect of a surface

In our model, an unbounded medium was considered, and the resultant motion gave rise to the perfect cancelation in the measurement of prompt gravity changes. If a realistic

finite Earth model is considered, its free surface may alter the ground acceleration because additional deformation could occur to satisfy the traction-free boundary condition. As a result, the perfect cancelation might break. Modeling of the prompt gravity change for a body with the free surface is discussed in the framework of the normal mode theory, and much smaller signal levels than the prediction of *Harms et al.* [2015] are expected [*Heaton,* 2017; *Montagner,* private communication]. Very recently, Vallee et al. (2017) reported the identification of the prompt gravity waveforms from the 2011 Tohoku-Oki earthquake. They employed an elastic wave propagation simulation to synthesize the theoretical waveforms of both the prompt gravity change and the ground acceleration in a half-space, and identified the simulated waveforms in observed data recorded by ten broadband seismometers. In this context, the very slight trends found in the F-net and Hi-net stacked traces may reflect the free surface effect.

## 4.5 Toward definite detection of earthquake-induced gravity signals using a gravity-gradient sensor

We have shown that the prompt gravity signal is difficult to be recorded with instruments measuring the relative motion between an inertial mass and the attached ground, such as gravimeters, seismometers, and tiltmeters. However, the possibility remains in terms of the gravity-gradient measurement. Spatially inhomogeneous gravity field induces tidal deformation of an object or spatial strain (Figure 24), which are observable even if the observer moves with acceleration of the gravity field. In this sense, the general expression for the gravity changes we derived in Chapter 2 (eqation 10, 18) may no longer useless for the signal detection, but the expression for the
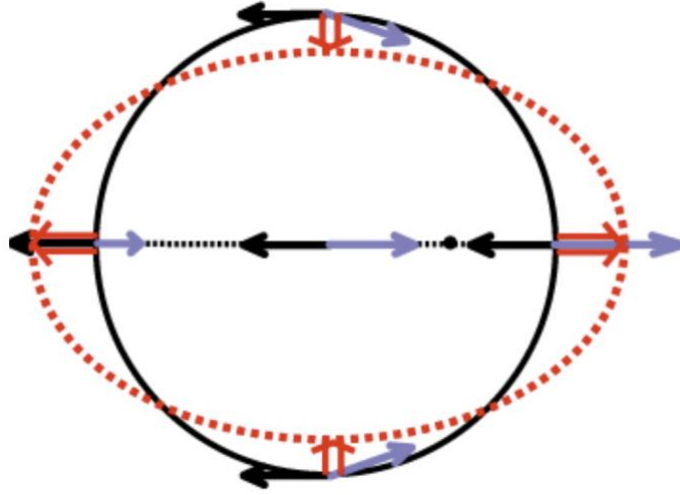
Figure 24. An example of tidal deformation of an object: the Earth tidally deformed by gravity forces due to the Sun and Moon (Figure from the internet).

gravity-gradient changes (equation 15, 19) is still useful. Our formula relies on the elastodynamic Green's function that is familiar to seismologists.

Detecting very small perturbations of the gravity gradient has been a challenge for detecting gravitational waves from space. Recently, *Abbott et al.* [2016] observed the gravitational waves using laser interferometers in a high frequency range from tens to hundreds of Hz. New state-of-the-art instruments, such as torsion bar antennas (TOBA) [*Ando et al.*, 2010; *Shoda et al.*, 2014, Figure 25] are being developed. The instrument intends to observe a spatial strain through the tidal deformation of the crossing bars. The existing proto-type TOBA attained a $10^{-8}$ s$^{-2}$ sensitivity within a low frequency range of 0.01–1 Hz [*Shoda et al.,* 2014]. The predicted signals are $10^5$ times smaller, but the next-generation TOBA will attain enough sensitivity to detect prompt earthquake signals. Prompt earthquake detection is awaiting such ultra-sensitive sensors.
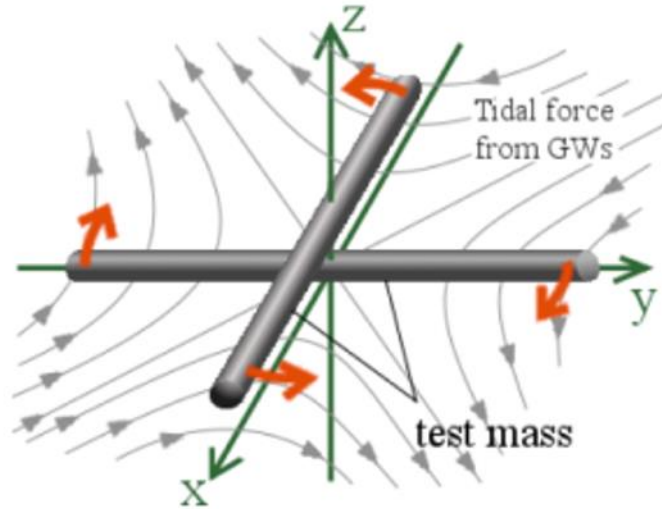
Figure 25. Schematic illustration of torsion bar antennas (TOBA; *Ando et al.,* 2010; *Shoda et al.,* 2014). This instrument aims to detect the spatial strain through tidal deformation of the two suspended bars.

# 5 Conclusions

We showed that the predicted prompt signals were identified in neither our band-pass filtering nor our stacking analysis. Analyses of the three different types of sensors all yielded the same negative detection, implying that these results are reliable. Our analyses suggest that there is an obvious discrepancy between the theoretical prediction and the data we have used. Our results conflict with the previous study of *Montagner et al.* [2016] claiming the consistency of their statistical result with the theory of *Harms et al.* [2015]. We speculated that the model signals were overestimated and that the actual intensities were much smaller than those predicted. In this context, our results confirmed that the upper limit of relevant signals recorded in the data was lower than $0.01 \times 10^{-8}$ m/s$^2$.

To interpret the absence of prompt signals, we investigated the effect of self-gravity deformation on measurements of gravitational acceleration. We solved the elastodynamic equation of motion loaded by the prompt gravity changes and obtained the resultant displacement accelerations. We then developed an observation model incorporated with the motion of the observation ground induced by self-gravity. The model showed that the inertial force originating from the resultant ground motion cancels out the gravitational force acting on a sensor mass before the arrival of *P* waves, leading to a null signal in the sensor output. Our theory verified the absence of earthquake-induced prompt gravity changes using inertial sensors.

To close, we discussed the intrinsic nature of gravity-induced elastic deformation. Instantaneous gravity changes necessarily accompany a temporary free fall because the elastic traction is zero between the event onset and the *P* wave arrival. What we call Einstein's elevator inevitably appears on Earth, and it is the manifestation of

intrinsic elasticity that has been unnoticed in classical normal mode theory. Although our theory disclosed the negative observability of the prompt gravity changes in acceleration, their gradients remain observable even in a moving system. For the future detection, the analytical expressions of theoretical gravity-gradient changes from a generalized source represented by a moment tensor can be used as template waveforms in time-series analysis.

# References

Abbott, B. P. et al. (2016), Observation of Gravitational Waves from a Binary Black Hole Merger, *Phys. Rev. Lett.*, *116*(6), 61102, doi:10.1103/PhysRevLett.116.061102.

Aki, K. and P.G., Richards (2002), *Quantitative Seismology*, 2nd. Ed., University Science Books, Susalito, California.

Ando, M., K. Ishidoshiro, K. Yamamoto, K. Yagi, W. Kokuyama, K. Tsubono, and A. Takamori (2010), Torsion-Bar Antenna for Low-Frequency Gravitational-Wave Observations, *Phys. Rev. Lett.*, *105*(16), 161101, doi:10.1103/PhysRevLett.105.161101.

Chu, R., S. Wei, D. V. Helmberger, Z. Zhan, L. Zhu, and H. Kanamori (2011), Initiation of the great Mw 9.0 Tohoku-Oki earthquake, *Earth Planet. Sci. Lett.*, *308*(3–4), 277–283, doi:10.1016/j.epsl.2011.06.031.

Han, S.-C., C.K. Shum, M. Bevis, C. Ji, and C. Kuo (2006), Crustal dilatation observed by GRACE after the 2004 Sumatra-Andaman earthquake, *Science*, *313*, 658-662

Han, S.-C., R. Riva, J. Sauber, and E. Okal (2013), Source parameter inversion for recent great earthquakes from a decade-long observation of global gravity field, *J. Geophys. Res. Solid Earth*, *118*, 1240-1267, doi:10.1002/jgrb.50116.

Harms, J. (2016), Transient gravity perturbations from a double-couple in a homogeneous half-space, *Geophys. J. Int.*, *205*(2), 1153–1164, doi:10.1093/gji/ggw076.

Harms, J., J. P. Ampuero, M. Barsuglia, E. Chassande-Mottin, J. P. Montagner, S. N. Somala, and B. F. Whiting (2015), Transient gravity perturbations induced by earthquake rupture, *Geophys. J. Int.*, *201*(3), 1416–1425, doi:10.1093/gji/ggv090.

Heaton. T. H. (2017), Correspondence: Response of a gravimeter to an instantaneous step in gravity, *Nat. Commun.*, 8, 66, doi:10.1038/s41467-017-01348-z.

Imanishi, Y. (2001), Development of a High-Rate and High-Resolution Data Acquisition System Based on a Real-Time Operating System, *J. Geod. Soc. Japan*, *47*(1), 52–57, doi:10.11366/sokuchi1954.47.52.

Imanishi, Y., T. Sato, T. Higashi, W. Sun, and S. Okubo (2004), A network of superconducting gravimeters detects submicrogal coseismic gravity changes., *Science*, *306*(5695), 476–8, doi:10.1126/science.1101875.

Montagner, J.-P., K. Juhel, M. Barsuglia, J. P. Ampuero, E. Chassande-Mottin, J. Harms, B. Whiting, P. Bernard, E. Clévédé, and P. Lognonné (2016), Prompt gravity signal induced by the 2011 Tohoku-Oki earthquake, *Nat. Commun.*, *7*, 13349, doi:10.1038/ncomms13349.

Okubo, S. (1992), Gravity and potential changes due to shear and tensile faults in a half-space, *J. Geophys. Res.*, 97, 7137-7144.

Shoda, A., M. Ando, K. Ishidoshiro, K. Okada, W. Kokuyama, Y. Aso, and K. Tsubono (2014), Search for a stochastic gravitational-wave background using a pair of torsion-bar antennas, *Phys. Rev. D*, *89*(2), 27101, doi:10.1103/PhysRevD.89.027101.

Tanaka, Y., S. Okubo, M. Machida, I. Kimura, and T. Kosuge (2001), First detection of absolute gravity change caused by earthquake, *Geophys. Res. Lett.*, *28*(15), 2979–2981.

Tonegawa, T., K. Hirahara, T. Shibutani, and K. Shiomi (2006), Upper mantle imaging beneath the Japan Islands by Hi-net tiltmeter recordings, *Earth, Planets Space*, *58*(8), 1007–1012, doi:10.1186/BF03352605.

Vallee, M., J. P. Ampuero, K. Juhel, P. Bernard, J.-P. Montagner, and M. Barsuglia (2017), Observations and modeling of the elastogravity signals preceding direct seismic waves, *Science, 358*, 1164-1168, doi: 10.1126/science.aao0746.

Wei, S., R. Graves, D. Helmberger, J. P. Avouac, and J. Jiang (2012), Sources of shaking and flooding during the Tohoku-Oki earthquake: A mixture of rupture styles, *Earth Planet. Sci. Lett.*, *333–334*, 91–100, doi:10.1016/j.epsl.2012.04.006.

## Appendix A. Displacement acceleration induced by the prompt gravity perturbation in an elastic full space

*Harms et al.* [2015] derived the expression for the prompt gravity perturbation $\delta \boldsymbol{g}$ induced by the seismic displacement $\boldsymbol{u}$. Here, we consider the displacement $\boldsymbol{\xi}$ induced by the prompt gravity perturbation $\delta \boldsymbol{g}$. As mentioned in section 3, we seek the unknown solution of $\boldsymbol{\xi}$ that satisfies the equation of motion with the given body force $\boldsymbol{f} = \rho \delta \boldsymbol{g}$.
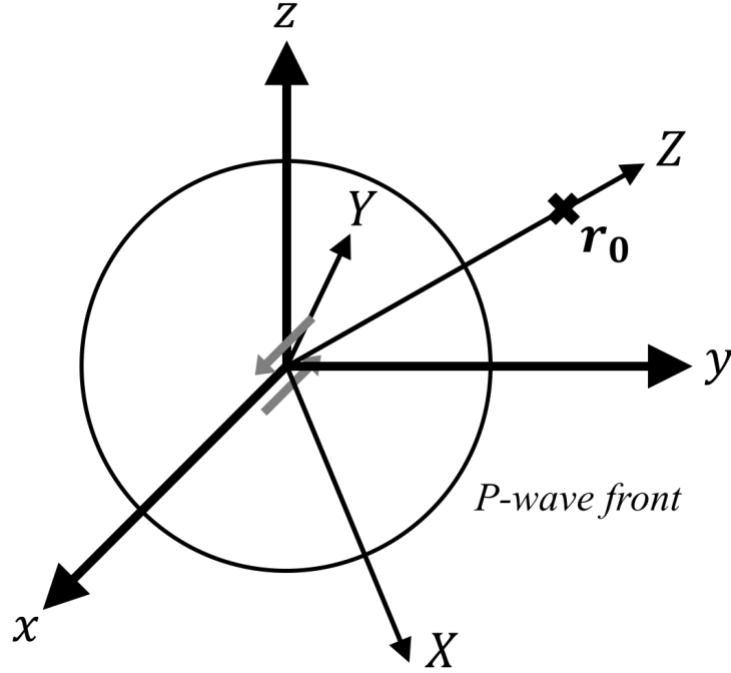
Figure 26. The fault slip at the origin and the source-based coordinates (*xyz*). The gravity change at the receiver location $\boldsymbol{r}_0$ outside the *P* wave front is induced by the distributed density perturbations inside the front. The *XYZ*-coordinates are based on the direction of $\boldsymbol{r}_0$.

We adopt a source-based Cartesian coordinate system (*xyz*) where we choose the origin at the location of a shear dislocation, the *x*-axis is parallel to the slip direction, and the *z*-axis is perpendicular to the fault plane (Figure 26).

The solution can be expressed using the representation theorem with the elastodynamic Green's function [*Aki and Richards*, 2002], where a displacement response to an impulsive body force is convoluted with the distributed gravity force $\rho \delta \boldsymbol{g}$ in both time and space:

$$\xi_n(\boldsymbol{r}_0, t) = \frac{1}{4\pi} \int_V dV(\boldsymbol{x}) \left[ (3\gamma_n'\gamma_m' - \delta_{nm}) \frac{1}{r'^3} \int_{r'/\alpha}^{r'/\beta} \tau \delta g_m(t - \tau) d\tau \right.$$

$$\left. + \frac{1}{\alpha^2} \gamma_n'\gamma_m' \delta g_m(t - r'/\alpha) - \frac{1}{\beta^2} (\gamma_n'\gamma_m' - \delta_{nm}) \delta g_m(t - r'/\beta) \right], \tag{A1}$$

where $\xi_n$ is the $n$-th component of $\boldsymbol{\xi}$,

$$\delta g_m(\boldsymbol{x}, t) = \left( -15\gamma_m\gamma_p\gamma_q + 3\gamma_m\delta_{pq} + 3\gamma_p\delta_{mq} \right.$$

$$\left. + 3\gamma_q\delta_{mp} \right) \frac{G}{r^4} \int_0^t dt' \int_0^{t'} dt'' M_{pq}(t''), \tag{A2}$$

$$M_{pq}(t) = \begin{pmatrix} 0 & 0 & 1 \\ 0 & 0 & 0 \\ 1 & 0 & 0 \end{pmatrix} M_0(t) =: A_{pq} M_0(t), \tag{A3}$$

$r = |\boldsymbol{x}|$, $r' = |\boldsymbol{r}_0 - \boldsymbol{x}|$, $\boldsymbol{\gamma} = \frac{\boldsymbol{x}}{r}$, and $\boldsymbol{\gamma}' = \frac{\boldsymbol{r}_0 - \boldsymbol{x}}{r'}$.

Our goal is to show that the solution of equation A1 satisfies $\ddot{\boldsymbol{\xi}} = \delta \boldsymbol{g}$ during the prompt period $0 < t < R/\alpha$. For this purpose, we conduct the coordinate transformation expressed below so that the volume integral of equation A1 can be solved. The moment tensor expression in equation A2 is useful for this analysis. We adopt the Cartesian coordinates (*XYZ*) where the receiver locates on the *Z*-axis. When the receiver location is expressed as $(R, \theta_0, \phi_0)$ in the spherical coordinates, *XYZ*-coordinates are realized by applying the two steps of rotation to xyz-coordinates: (i) $\phi_0$ rotation around the *z*-axis (ii) $\theta_0$ rotation around the *y'*-axis, which are expressed by

$$\text{(i) } R_z = \begin{pmatrix} \cos\phi_0 & \sin\phi_0 & 0 \\ -\sin\phi_0 & \cos\phi_0 & 0 \\ 0 & 0 & 1 \end{pmatrix} \text{ and (ii) } R_y = \begin{pmatrix} \cos\theta_0 & 0 & -\sin\theta_0 \\ 0 & 1 & 0 \\ \sin\theta_0 & 0 & \cos\theta_0 \end{pmatrix}.$$

In the *XYZ*-coordinates, the moment tensor $M_{pq}'(t)$ has its components as

$$M'_{pq}(t) = R_y R_z A_{pq} R_z^{-1} R_y^{-1} M_0(t)$$

$$= \begin{pmatrix} -\sin 2\theta_0 \cos\phi_0 & \sin\theta_0 \sin\phi_0 & \cos 2\theta_0 \cos\phi_0 \\ \sin\theta_0 \sin\phi_0 & 0 & -\cos\theta_0 \sin\phi_0 \\ \cos 2\theta_0 \cos\phi_0 & -\cos\theta_0 \sin\phi_0 & \sin 2\theta_0 \cos\phi_0 \end{pmatrix} M_0(t) \qquad \text{(A4)}$$

$$=: A'_{pq} M_0(t).$$

Inserting equation A4 into equation A2 and equation A2 into equation A1 yields the displacement $\Xi\big((R,0,0),t\big)$ in the *XYZ*-coordinates:

$$\begin{pmatrix} \Xi_1 \\ \Xi_2 \\ \Xi_3 \end{pmatrix} = \begin{pmatrix} 6A'_{13} \\ 6A'_{23} \\ -9A'_{33} \end{pmatrix} \frac{G}{R^4} \int_0^t dt' \int_0^{t'} dt'' \int_0^{t''} dt''' \int_0^{t'''} dt'''' M_0(t''''). \qquad \text{(A5)}$$

One finds that the right-hand side includes the second integral of the prompt gravity perturbation. equation A5 can be expressed in the original coordinates (*xyz*) as

$$\begin{pmatrix} \xi_1 \\ \xi_2 \\ \xi_3 \end{pmatrix} = R_z^{-1} R_y^{-1} \begin{pmatrix} \Xi_1 \\ \Xi_2 \\ \Xi_3 \end{pmatrix}$$

$$= \begin{pmatrix} -30\gamma_1^2\gamma_3 + 6\gamma_3 \\ -30\gamma_1\gamma_2\gamma_3 \\ -30\gamma_1\gamma_3^2 + 6\gamma_1 \end{pmatrix} \frac{G}{R^4} \int_0^t dt' \int_0^{t'} dt'' \int_0^{t''} dt''' \int_0^{t'''} dt'''' M_0(t''''). \qquad \text{(A6)}$$

Taking the second derivative with respect to time, the displacement acceleration is found to be equal to the applied prompt gravity perturbation:

$$\ddot{\xi}_m(\boldsymbol{r}_0,t) = (-30\gamma_1\gamma_3\gamma_m + 6\gamma_1\delta_{m3} + 6\gamma_3\delta_{m1}) \frac{G}{R^4} \int_0^t dt' \int_0^{t'} dt'' M_0(t'')$$

$$= \delta g_m(\boldsymbol{r}_0,t). \qquad \text{(A7)}$$

## Chapter 4. General conclusion

第二章では、点食い違いが引き起こす理論重力波形を導いたHarms et al. (2015)のモデルを拡張し、シングルフォースまたはモーメントテンソルが引き起こす理論重力変化及び理論重力勾配変化の全時間領域での表現を得た。その時空間的性質を調べるため、代表的な３つの震源 (a) ダブルカップル：例として2011年東北沖地震、(b) シングルフォース：1980年セントヘレンズ火山噴火、及び (c) 等方爆発に対して重力変化と重力勾配変化の理論波形を合成した。その結果、理論重力変化及び理論重力勾配変化が持つ特異的な距離依存性や、M9規模の超巨大地震による即時重力変化の観測可能性が明らかになった。

第三章の前半部（データ解析）では、第二章で合成した理論波形と観測波形とを直接比較し、2011年東北沖地震による重力変化を加速度データの中から探した。三種類の測器によるデータに対してバンドパスフィルタ処理や多点スタッキング処理を行ない、信号ノイズ比は十分に改善したが、理論から期待される波形は同定できなかった。これはHarms et al. (2015) の単純な理論と観測データとの矛盾を示している。

第三章の後半部（新たな観測モデル構築）では、この解析結果を解釈するため、地球の自己重力の効果が重力計測を行う観測サイト周辺の弾性変形を通して重力計測に与える影響を定量的に調べた。我々は、無限均質等方弾性媒質において、地震による即時重力変化が媒質に体積力として作用することで引き起こされる媒質の運動を動弾性体の運動方程式を解くことで導き、P波到達前の観測サイトの変位の解析解を得た。その結果は非常に興味深く、P 波到達前の

観測サイトの地動加速度はそこに働く即時重力変化と完全に一致するというものであった。これは重力測定において、重力計センサーの計測質量に働く即時重力変化は地動加速度による慣性力によって完全に打ち消され、センサーの出力には一切現れないことを意味する。すなわち、地震発生に伴い即時重力変化それ自体は生じるが、観測サイトもそれにより弾性変形を起こし同一の加速度で運動する結果、測定装置は即時重力変化に対して感度を失うのである。我々がデータ解析で用いた超伝導重力計、地震計、傾斜計はいずれも観測装置とテストマスとの相対運動に依存した装置であり、即時重力変化に対して感度を持たないことになる。このことは我々がデータ解析から得た結果と整合的である。

　また我々は、地震時において解析的に導いたこの「P波到達前の媒質の自由落下運動」とも呼べる弾性体の運動が、実は地震時に限らず任意の密度変化の出現に対しても成り立つことを、重力相互作用と弾性体の運動方程式の性質から示した。その意味でこの一時的な自由落下運動は弾性体の本質的性質であると言える。

　我々が構築した新たな観測モデルは無限均質媒質を仮定しているが、表面を持つ現実的な有限媒質では、対称性の破れから即時重力変化と地動加速度による慣性力との完全キャンセルは成り立たないと考えられる。我々のデータ解析のスタック波形が示すP波前のわずかなトレンドはこの表面の効果を反映している可能性があり、その効果を取り入れたより精緻な理論の構築が待たれる。10月のERI-IPGPワークショップにおける議論では、IPGPの学生が自由振動モデルに基づいたコードを作成し、地球の変形と重力場を完全にカップルさせた形で地震による即時重力変化と地動変位の理論波形を作れるようになったことが

紹介された (Montagner, private communication)。そのコードを使って我々の解析結果を理論と合わせることが、今後の研究として真っ先に行えることである。また、重力の空間勾配あるいは空間歪は運動する系でも打ち消されないため我々の新たな観測モデルにおいても依然として観測可能であり、第二章で導いた理論重力勾配変化の一般表現は将来の信号検出においてテンプレート波形作成のために有用である。

　最後に、本論文の第二章はGeophysical Journal Internationalへの投稿原稿を改変して作成し、また第三章は Journal of Geophysical Research: Solid Earthへの投稿原稿を改変して作成した。また、本研究の内容は2015年、2016年、及び2017年の日本地震学会秋季大会において延べ5件の発表を行なった。その予稿をSupplement に付録としてつける。

## Acknowledgement

## Supplement

付録内容

・日本地震学会秋季大会予稿5件

木村将也・亀伸樹・綿田辰吾・大谷真紀子・新谷昌人・今西祐一・安東正樹、「重力で地震発生を捉える -断層の動的破壊に伴う重力変化検出の理論的検討-」、神戸、2015年10月

木村将也・亀伸樹・綿田辰吾・大谷真紀子・新谷昌人・今西祐一・安東正樹、「重力で地震発生を捉える(2) -地震重力変化の理論波形を用いたデータ解析-」、名古屋、2016年10月

木村将也・亀伸樹、「重力で地震発生を捉える(3) -重力変化と重力勾配変化の理論記象のモーメントテンソル表現-」、名古屋、2016年10月

木村将也・亀伸樹・綿田辰吾・大谷真紀子・新谷昌人・今西祐一・安東正樹・功刀卓、「重力で地震発生を捉える(4) -データ解析における信号不検出とその物理的解釈-」、鹿児島、2017年10月

木村将也・亀伸樹、「重力で地震発生を捉える(5) -地震即時重力変化による弾性変形場の理論解析-」、鹿児島、2017年10月

・0.001-0.03 Hz バンドパスフィルタ処理後のF-net広帯域地震計記録一覧

全70点、縦線は発震時刻 05:46:24.3 (UTC)

・0.001-0.03 Hz バンドパスフィルタ処理後のHi-net傾斜計記録一覧

非地震発生時の振幅がフィルタ後に$10^{-9}$ m/s$^2$以下の点のみ（東西成分137点、南北成分181点）

# 重力で地震発生を捉える

### -断層の動的破壊に伴う重力変化検出の理論的検討-

#木村将也（東大理地惑）・亀（伸樹）・綿田辰吾・大谷真紀子・新谷昌人・今西祐一（東大地震研）・安東正樹（東大院物理）

Detecting Gravity Change due to Earthquake Dynamic Rupture
- Feasibility study based on theoretical modeling -

#Kimura, M. (EPS, Univ. Tokyo), Kame, N., Watada, S., Ohtani, M., Araya, A., Imanishi, Y. (ERI), Ando, M. (Dept. Phys., Univ. Tokyo)

**1. はじめに** 現在、最も早く地震発生を知る手段は地震計[1]によるP波初動の検知である。地震波P波速度が数km/sのオーダーであるることを鑑みれば、震源が地下20kmの場合、地震発生から初動検知まで最低でも3s程度かかることになる。一方、断層すべりより引き起こされる重力変化は光速度で媒質中に密度変化が生じ、これにより伝わる（図1）。これにより伝わる速度（$c=3.0×10^8$ m/s）で伝わる。地震波を伝わる。地震波は日本中でほぼ同時に、地震発生以降遅延時間ゼロで到着することになる。もし、地震発生を重力変化で捉えることができれば地震の早期検知に役立つ。本講演では、単純な点震源の理論モデルを用いて2011年東北地震から期待される重力変化形を評価し、重力変化による地震の早期検知の可能性を検討する。

**2. 理論モデル** 全無限弾性体中に置かれたダブルカップルの点震源が引き起こす重力変化のHarmsらの理論モデル[2]を拡張して用いた。彼らは地震発生時刻からP波到着時刻までの重力変化に注目し対応する即時項を導出した。即時項の立ち上がりは地震モーメント関数$M_0(t)$から生成される関数$I_2[M_0](t)$に比例することが示されて我々は、地震発生時刻からP波初動着時刻を経て静的変形に至るまでの全時系列の重力変化形の理論式（ベクトル3成分）を導出した。これにより地震破壊と波動伝播の全過程の中での即時項の位置づけを明らかにする。

**3. 2011年東北地震から期待される重力変化の時系列** 地震波解析から得られた地震モーメントレート関数を用いて超伝導重力計観測点3ヶ所（水沢・松代・神岡）における重力変化理論波形3成分$(dg_X, dg_Y, dg_Z)$を即時項から合成した。重力変化は地震発生時刻から即時項に、しかし非常に緩やかに

立ち上がる。立ち上がりを時間のべき乗で近似すると$4<n<5$であった。$dg_Z$成分に注目すると、例えば神岡（震源距離515km、P波到着時刻74s）では、P波初着時刻に3$\mu$gal、静的最終着時刻が17$\mu$galとなった（1$\mu$gal=$10^{-8}$ m/s$^2$）。超伝導重力計は1$\mu$galの変化に対して十分な分解能を持つが、神岡での重力波形記録を見てみると微動ノイズの振幅が10～20$\mu$gal程度であり、重力の即時変化を同定することはできなかった。即時項の最大値の日本全体の分布を計算した所、最大5$\mu$gal程度になる。更に、我々は重力の偏差（テンソル6成分）についても期待される変化化の最終着時刻、即時項が$10^{-13}$/s$^2$程度、静的最終最大変化は現在$10^{-8}$/s$^2$。即時項の最大値を調べた所、重力歪計TOBA($f=0.1$Hz)[3]の感度は現在$10^{-8}$/s$^2$[4]、次世代で$10^{-13}$/s$^2$であり次世代機において検知可能性が視界に入る。

**4. まとめ** 重力変化と重力差変化の期待される信号差変化レベルを押さえることができた。検知にはノイズレベルの軽減が必須である。既存の重力計のS/N向上に関し免震合への設置やアレイ観測が考えられる。
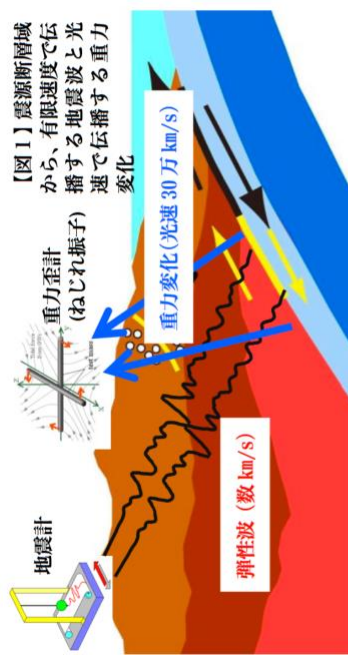


【図1】震源断層域から、有限速度で伝播する地震波と光速で伝播する重力変化

重力歪計（ねじれ振子）
重力変化（光速 30 万 km/s）
弾性波（数 km/s）
地震計

参考文献
[1] http://www.hinet.bosai.go.jp/about_earthquake/sec9.1.html. 地震計の原理.
[2] Harms, J. et al., 2015. Transient gravity perturbations induced by earthquake rupture, Geophys. J. Int., 201, 1416–1425, doi: 10.1093/gji/ggv090.
[3] Ando, M. et al., 2010. Torsion-bar antenna for low-frequency gravitational-wave observations, Phys. Rev. Lett., 105, 161101.
[4] Shoda, A., 2014. Development of a high-angular-resolution antenna for low-frequency gravitational-wave observation, Dr. Sc. Thesis, the University of Tokyo.

# 重力で地震発生を捉える(2)
## － 地震重力変化の理論波形を用いたデータ解析 －

#木村将也・亀伸樹・綿田辰吾（東大地震研）・大谷真紀子・新谷昌人・今西祐一（東大地震研）・安東正樹（東大院物理）

**Detecting Gravity Change due to Earthquake Dynamic Rupture (2)
- Observed data analysis based on the theoretical seismic gravitogram -**

#Kimura, M., Kame, N., Watada, S. (ERI), Ohtani, M. (AIST), Araya, A., Imanishi, Y. (ERI), Ando, M. (Dept. Phys., Univ. Tokyo)

1. はじめに　地震が発生すると、地震波の伝播に伴い媒質中に密度変化が生じ、この密度変化が引き起こす重力変化は光速度で伝わる。これは地震波に比して圧倒的な速度であり、重力変化は実質的に地震発生時刻から遅延時間ゼロで到着することになる。もし、地震発生を重力変化で捉えることができれば地震の早期検知に役立てることができる。我々は重力変化の弾性体モデルを用いて2011年東北地震から期待される重力変化について考察してきた（木村・他、2015、地震学会）。本研究では、この理論波形をもとに実際の観測データにおいて信号検出解析を行なった。

2. 理論モデル　全無限弾性体中でダブルカップル点震源が引き起こす重力変化のHarms et al. (2015)の理論モデル（即時項）を用いる。地震発生時刻からP波到達時刻までの重力変化は、その後の変形に至るまでの全時系列の静的変形を含み、その各成分を合成することができる（ただし地動に起因する分は含まない）。重力理論波形 (gravitogram) の$(x, y, z)$の各成分を合成することができる（た

3. 2011年東北地震から期待される重力変化の時系列と空間分布　超伝導重力計が設置されている神岡で期待される重力変化の理論波形3成分を図1に示す。重力変化は地震発生時刻から即時に、しかし緩やかに立ち上がる。日本全体での計算から P波到達直前での鉛直重力変化は陸域の広範囲で3μgal程度となる。

4. 理論波形にもとづく観測波形解析の準備的結果　2011年東北地震の際に神岡で記録された超伝導重力計の波形（図2、40Hzサンプリング）を解析した。ここで期待される重力変化（図1）は3.5μgal程度である。そこで、0.1Hz LPF処理によってノイズを±0.5μgal程度まで低減させ

た（図3）。現段階では、対応する信号は含まれていないように見える。本研究では、この神岡での観測データの準備的解析の結果をふまえて、日本で利用可能な超伝導重力計データ（松代・水沢）の解析を行なう。また、F-net広帯域地震計（全国約70点、20Hzサンプリング、速度データを加速度に変換して解析）、およびHi-net傾斜計（約1000点、20Hzサンプリング、加速度データ）のデータを用いても、期待される地震重力変化の検出を試みる。



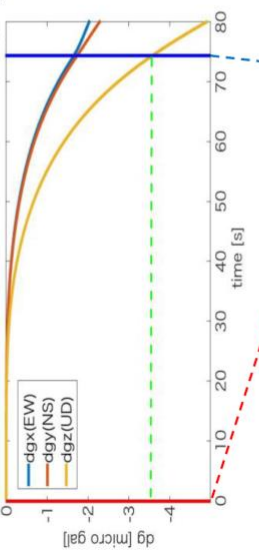図1：2011年東北地震による神岡での重力変化理論波形3成分（赤線）。t=0（赤線）を地震発生時刻とし、t=74s（青線）で神岡へP波到達。



図2：2011年東北地震の際に神岡超伝導重力計で記録された鉛直重力波形。UTC 05:46:18（赤線）で地震発生、05:47:32（青線）でP波到達。


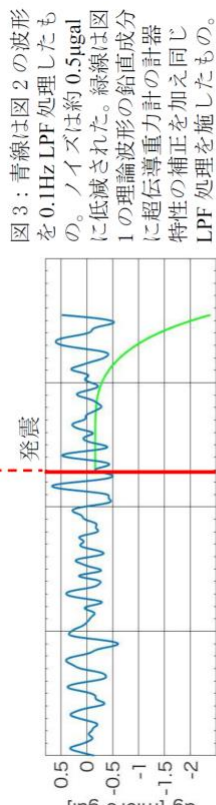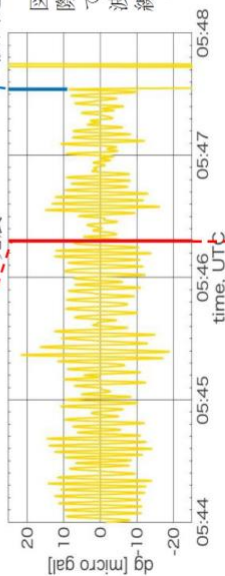
図3：青線は図2の波形を0.1Hz LPF処理したもの。ノイズは約0.5μgalに低減された。緑線は図1の理論波形の鉛直成分に超伝導重力計の計器特性の補正を加えつつ同じLPF処理を施したもの。

# 重力で地震発生を捉える(3)
## －重力変化と重力勾配変化の理論記象のモーメントテンソル表現－

### Detecting Gravity Change due to Earthquake Dynamic Rupture (3)
### - Moment tensor representation of seismic gravitogram and gravitogradiogram -

#Kimura, M., Kame, N. (ERI)
#木村将也・亀伸樹 (東大地震研)

## 1. はじめに

Harms *et al.* (2014)は、断層の動的破壊に伴う過渡的な重力変化について考えた。無限等方均質媒質中に置かれた $x_1$-$x_3$ 軸方向のダブルカップル震源による密度変位場 $u(x, t)$ のボソテンシャル表現からスタートし、その結果として生じる密度変化場 $\delta\rho(x, t)$ の評価を経て、重力ポテンシャル変化 $\delta\psi(x, t)=-4\pi\rho G\phi(x, t)$ を導いた。すなわち、動的破壊に起因する密度変化からもたらされる重力ポテンシャルの変化が、地震波の (P波) スカラーポテンシャル $\phi(x, t)$ と等価 (定数倍異なる) になる。この関係式は弾性体の運動方程式を満たすすべ意の波動場で有効であり、「スカラーポテンシャルが既知の波動場においては、ただちに重力応答を評価する」ことを意味する。本研究ではこの性質を利用して、任意の震源に対する重力変化の理論記象の表現を導く。

## 2. 重力変化理論記象のモーメントテンソル表現

我々は、一般的な震源の記述方法であるモーメントテンソル震源 $M_{pq}(t)$ から放射される地震波の問題を考える (Aki & Richards, 2002)。弾性波動場のポテンシャル表現から戻り、対応する重力の時間変化の解析解、すなわち重力変化 $\delta g_n(x, t)$ の理論記象 (ベクトル 3 成分) を導いた (右辺第一項は $t=0$ から立ち上がる即時項、他は遅延項)。

$$\delta g_n(x, t) = 4\pi\rho G[M_{pq} * G^\phi_{pq,n}]$$

$$= -(15\gamma_n\gamma_p\gamma_q - 3\gamma_n\delta_{pq} - 3\gamma_p\delta_{qn} - 3\gamma_q\delta_{np})\frac{G}{r^4}I_2[M_{pq}](t, \frac{r}{\alpha})$$

$$+ (6\gamma_n\gamma_p\gamma_q - \gamma_n\delta_{pq} - \gamma_p\delta_{qn} - \gamma_q\delta_{np})\frac{G}{\alpha^2 r^2}M_{pq}(t - \frac{r}{\alpha})$$

$$+ (\gamma_n\gamma_p\gamma_q)\frac{G}{\alpha^3 r}\dot{M}_{pq}(t - \frac{r}{\alpha}),$$

$$I_2[M_{pq}](t, \frac{r}{\alpha}) = \int_0^{r/\alpha} \tau M_{pq}(t - \tau) d\tau.$$

## 3. 重力勾配変化理論記象のモーメントテンソル表現

重力勾配は計測可能な重力変化に対して、理論記象 $(\nabla g = \dot{h}(x, t):$ひずみ加速度。3x3 のテンソル) の各成分は以下の表現となる (右辺第一項が即時項、他は遅延項)。

$$\ddot{h}_{mn} = \frac{\partial \delta g_n}{\partial x_m} = (4\pi\rho G)(M_{pq} * G_{np,qm}) = (-4\pi\rho G)u^\phi_{n,m}$$

$$= [R_5 \times \frac{G}{r^5}I_2[M_{pq}](t, \frac{r}{\alpha}) + R_3 \times \frac{G}{\alpha^2 r^3}M_{pq}(t - \frac{r}{\alpha})$$

$$+ R_2 \times \frac{G}{\alpha^3 r^2}\dot{M}_{pq}(t - \frac{r}{\alpha}) + R_1 \times \frac{G}{\alpha^4 r}\ddot{M}_{pq}(t - \frac{r}{\alpha})],$$

$R_5 = 105\gamma_n\gamma_p\gamma_q\gamma_m - 15(\delta_{mn}\gamma_p\gamma_q + \delta_{mp}\gamma_n\gamma_q + \delta_{mq}\gamma_n\gamma_p) - 15(\delta_{pq}\gamma_n\gamma_m + \delta_{qn}\gamma_p\gamma_m + \delta_{np}\gamma_q\gamma_m) + 3(\delta_{pq}\delta_{nm} + \delta_{np}\delta_{qm})$, $R_3 = -45(\gamma_n\gamma_p\gamma_q\gamma_m) + 6(\delta_{mn}\gamma_p\gamma_q + \delta_{mp}\gamma_n\gamma_q + \delta_{mq}\gamma_n\gamma_p) + 6(\delta_{pq}\gamma_n\gamma_m + \delta_{qn}\gamma_p\gamma_m + \delta_{np}\gamma_q\gamma_m) - (\delta_{pq}\delta_{nm} + \delta_{np}\delta_{qm}), R_2 = -10\gamma_n\gamma_p\gamma_q\gamma_m + (\delta_{mn}\gamma_p\gamma_q + \delta_{mp}\gamma_n\gamma_q + \delta_{mq}\gamma_n\gamma_p) + (\delta_{pq}\gamma_n\gamma_m + \delta_{qn}\gamma_p\gamma_m + \delta_{np}\gamma_q\gamma_m), R_1 = -\gamma_n\gamma_p\gamma_q\gamma_m$.

## 4. 等方爆発を例に

等方爆発により引き起こされる重力変化を考える。モーメントテンソルは $M_{11}=M_{22}=M_{33}=M_0(t)$ であり、問題の対称性より、結果は震源距離と動径方向ベクトルのみに依存する。密度変化は

$$\delta\rho(x, t) = -\delta(r)\frac{M_0(t)}{\alpha^2} + \frac{1}{4\pi\alpha^4 r}\ddot{M}_0(t - \frac{r}{\alpha}),$$

となる。また、対応する重力変化は

$$\delta g(x, t) = \frac{G}{r^2}\frac{M_0(t - \frac{r}{\alpha})}{\alpha^2}e_r + \frac{G}{r}\frac{\dot{M}_0(t - \frac{r}{\alpha})}{\alpha^3}e_r$$

となる。密度変化は震源で質量 $M_0/\alpha^2$ の吸い込みとなる一方、同量の正の密度変化が P 波として放射される。重力応答は即時項 $I_2[M_{pq}](t)$ を含まず P 波遅延延で伝わる。なぜなら、P 波到着前には震源での質量の吸い込みと P 波の球状対称な正の密度変化が打ち消し合い、P 波フロントの外側から見たときの実効的な質量変化がゼロであるからである。P 波通過後は、吸い込みからの引力と P 波質量変化からのモーメントテンソルを解析すると考える。この例のように、我々のモーメントテンソル表現は、地震、火山現象に起因する過渡的な重力・重力勾配の変化を担う。今後の重力観測に依拠した研究に資すると考える。

# 重力で地震発生を捉える(4)
## ― データ解析における信号不検出とその物理的解釈 ―

#木村将也・亀伸樹・綿田辰吾(東大地震研)・大谷真紀子(産総研)・新谷
昌人・今西祐一(東大地震研)・安東正樹(東大物理)・功刀卓(防災科研)

## Detecting Gravity Change due to Earthquake Dynamic Rupture (4)
## - Absence of earthquake-induced prompt gravity signals in data and its
## physical interpretation -

#Kimura, M., Kame, N., Watada, S. (ERI), Ohtani, M. (AIST), Araya, A., Imanishi, Y.
(ERI), Ando, M. (Dept. Phys., Univ. Tokyo), Kunugi, T. (NIED)

**1. はじめに** 地震断層から放射される地震波は媒質の密度変化を引き起こし、それに起因する重力変化は光速度で伝わる。実質的に遅延時間ゼロのこの即時重力変化を実際に検出できれば、地震の即時検知に有効である。我々はこれまで、既存の弾性体モデルから期待される重力変化の理論波形を用いて2011年東北沖地震からの即時重力変化の信号検出を試みてきた(木村他、地震学会2015, 2016a, b)。本研究では、多点観測データのスタッキング解析において十分な S/N 比を達成してもなお観測データに即時重力信号が見つからないことを確かめた。これを受け付信号の不在を説明する新たな理論モデルを構築した。

**2. 既存の理論モデル** 我々のデータ解析は、全無限弾性体中での地震の点震源が引き起こす重力変化についての Harms *et al.* (2015)のモデルに依拠する。地震発生時刻から P 波到達時刻までの即時重力変化(鉛直成分)の理論波形を図1に示す。神岡観測点において期待される重力変化(鉛直成分)の理論振幅は超伝導重力計で検出可能な値である。

**3. 理論波形にもとづく観測波形解析** 2011年東北沖地震の際に神岡と松代で記録された超伝導重力計の波形(40 Hz サンプリング)を解析し、2. の理論モデルから期待される重力信号を探した。0.001-0.1 Hz バンドパスフィルタによってノイズは十分に軽減されたが、信号は一切検出されなかった(図2)。F-net 広帯域地震計(全国約70点)および Hi-net 傾斜計(約800点)のデータに対してのみ多点スタッキング処理も施したが、やはり信号は存在しなかった(図3)。

**4. 地動加速度を考慮に入れた新たなモデルの構築** この理論と観測の不一致

を解決するために、即時重力変化が引き起こす弾性変形が重力測定に与える影響を考察する。我々は背景重力のない全無限均質媒質において、即時重力変化が体積力として作用した結果生じる弾性変位の解析表現を導出し、P 波到達前の観測点の地動加速度はそこに働く即時重力変化と一致することを見いだした。これは重力測定において、即時重力変化は地動による慣性力で完全に打ち消されることを意味する。即時重力変化は生じているが、重力計が加速度運動する結果、測定装置の出力には反映されないという我々の新たな観測モデルの説明は、3. の結果と整合的である。
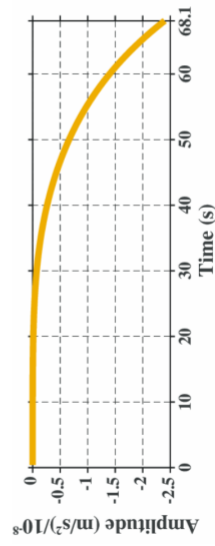
図1:2011年東北沖地震による神岡での重力変化の理論波形(鉛直成分を上向き正)。$t=0$ を地震発生時刻とし、$t=68.1$ s で神岡へ P 波到達。
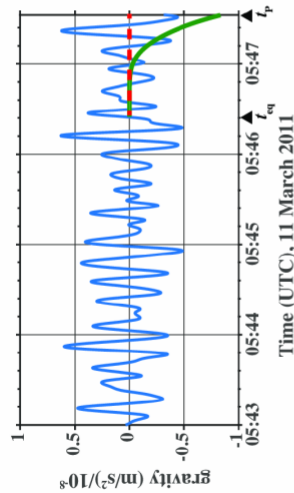
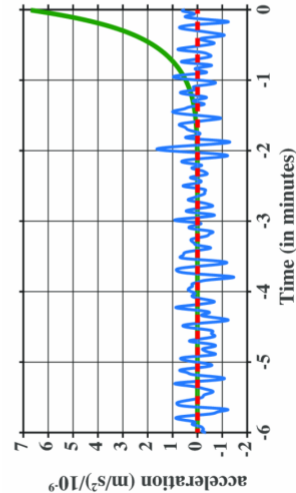図2:2011年東北沖地震の際に神岡超伝導重力計で記録された鉛直重力波形(青線)と期待される理論波形(緑線)。いずれも 0.001-0.1 Hz バンドパスフィルタ後。赤点線は我々の新たなモデルによる理論波形。

図3:F-net 広帯域地震計の記録を各観測点の P 波到達時でスタックした波形(青線)と、同様に各観測点での理論波形をスタックした波形(緑線)。いずれもバンドパスフィルタ後。赤点線は我々の新たなモデルによる理論波形。

# 重力で地震発生を捉える(5)
## －地震即時重力変化による弾性変形場の理論解析－

**Detecting Gravity Change due to Earthquake Dynamic Rupture (5)**
**- Theoretical analysis of elastic deformation due to earthquake-induced prompt gravity change -**

#Kimura, M., Kame, N. (ERI)
#木村将也・亀伸樹(東大地震研)

## 1. はじめに

我々は地震発生で引き起こされる実質的に遅延時間ゼロの即時重力変化の検出を試みてきたが、データ解析において信号は一切検出されなかった(木村・他、SSJ, 2017a)。Harms et al. (2015) は全無限弾性体中におかれた点震源が引き起こす、P波到達時までの即時重力変化の解析解 $\delta g(x, t)$ を導いた。そこで我々は、$\delta g(x, t)$ の計測において更に必要となる補正「観測点の地動加速度」について理論的に考察する。

## 2. 即時重力変化が引き起こす弾性変形場の導出

背景重力場のない全無限均質媒質において、地震による即時重力変化 $\delta g(x, t)$ が体積力として媒質に作用した際に引き起こされる、地震発生時刻からP波到達時刻までの観測点の地動加速度 $\xi(x, t)$ を導出する。地動変位場 $\xi(x, t)$ は以下の運動方程式を満たす(Aki and Richards, 2002)。

$$\rho \ddot{\xi}(x, t) = (\lambda + 2\mu)\nabla(\nabla \cdot \xi(x, t)) - \mu \nabla \times (\nabla \times \xi(x, t)) + f(x, t). \quad (1)$$

ここで $\rho$ は媒質の密度、$\lambda, \mu$ はラメ定数、$f(x, t) = \rho \delta g(x, t)$ である。即時重力変化 $\delta g(x, t)$ は既知であり、このとき変位場 $\xi(x, t)$ は表現定理を用いてグリーン関数と $\rho \delta g(x, t)$ との時空間の畳み込み積分で表現することができる。我々は、この積分を陽な形で得ることに成功した。結果は大変興味深く、かつ直感を解析的に実行し解を得ることは理論的には困難である。すなわち、P波到達以前の観測点の地動加速度 $\ddot{\xi}(x, t)$ は、その点での即時重力変化 $\delta g(x, t)$ と一致する。

$$\ddot{\xi}(x, t) = \delta g(x, t). \quad (2)$$

## 3. 地動加速度を考慮に入れた重力計測モデル

観測点に固定された重力計が加速度運動をすると、それによって重力計の試験質量に慣性力が作用し重力測定に影響を与える(図1)。重力計の出力 $s(t)$ は重力 $g(t)$ と地動加速度の差となる、$s(t) = g(t) - \ddot{\xi}(t)$。式(2)から、即時重力変化は地動加速度による慣性力で打ち消され、その結果、重力計は即時重力変化に対して感度を失うことになる。

## 4. 地球上至る所で自由落下する重力観測点：アインシュタインエレベーターの一時的な出現

式(2)は媒質の各点が即時重力変化によって自由落下することを意味しているが、これは我々の直感に反する。なぜなら式(2)で求まる変位は空間的に非一様であり、そのような変形により生じるトラクション(式(1)右辺第1項及び第2項)は、重力変化 $\delta g(x, t)$ の働く方向から運動をするはずだからである。我々は、この自由落下運動が、即時重力変化に対する弾性体の本質的な応答であることを見いだした。物理的には、重力相互作用の空間的特性($1/r^2$(減衰する発散場))により、式(2)は発散ゼロかつ回転ゼロを満たし、式(1)において確かにトラクション項ゼロとなることが理解できる。

## 5. 将来の即時地震検知へ向けて

(重力の空間勾配)はセンサーが加速度運動をしても計測可能である。将来の地震即時検知の実現に向けて、我々はモーメントテンソル震源に対する地震重力勾配波形の理論式を導いた。現在、アインシュタイン重力波の検出を目指しておりアンテナ型ねじり重力計が開発されている(Ando et al., 2010; Shoda et al., 2014)。これは1–100秒帯域に感度を持ち、地震重力変化の検出にも適している。

**Earth**

$\xi$

$M$

$f^i = -M\ddot{\xi}$

$f^g = Mg$
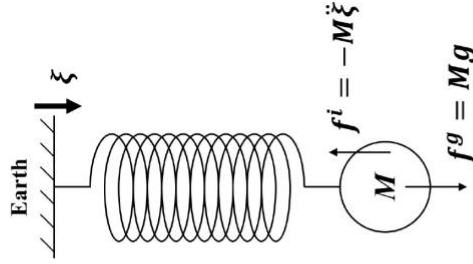
図1 重力測定の原理。質量に作用する重力と測定器の加速度運動による慣性力。

Time after 05:00 11 March 2011 (min)

NKG
WTR
NOP
TGA
SHR
KNP
NAA
KNM
KNY
HID
KSR
URH
WJM
FUJ
SGN
KMU
ONS
KZK
ADM
TMR
ASI
GJM
TSK
SBT
YMZ
KSK
HRO
TYS
KSN

2 nm/s²

40    42    44    46    48    50    52

Time after 05:00 11 March 2011 (min)

IGK

TKO

OKW

AOG

HJO

NMR

KZS

IMG

TTO

JIZ

MMA

15 nm/s$^2$

40　　　42　　　44　　　46　　　48　　　50　　　52

Time after 05:00 11 March 2011 (min)

Time after 05:00 11 March 2011 (min)

Time after 05:00 11 March 2011 (min)

Time after 05:00 11 March 2011 (min)

Time after 05:00 11 March 2011 (min)

Time after 05:00 11 March 2011 (min)

KORH.LN
KKIH.LN
KYAH.LN
MSMH.LN
SUKH.LN
TMNH.LN
NRAH.LN
SDWH.LN
YABH.LN
UMIH.LN
NANH.LN
TGOH.LN
KWMH.LN
KIWH.LN
YGNH.LN
SGWH.LN
KIKH.LN
HGIH.LN
MTOH.LN
NGTH.LN
OOTH.LN
MTMH.LN
MICH.LN
TSSH.LN
IKNH.LN
OOZH.LN
SKIH.LN
KWBH.LN
HISH.LN
TBEH.LN

5 nm/s$^2$

40    42    44    46    48    50    52

Time after 05:00 11 March 2011 (min)

Time after 05:00 11 March 2011 (min)

Time after 05:00 11 March 2011 (min)

Time after 05:00 11 March 2011 (min)

5 nm/s²

Time after 05:00 11 March 2011 (min)

Time after 05:00 11 March 2011 (min)